

THS

This is to certify that the thesis entitled

MOLECULAR TAGGING VELOCIMETRY MEASUREMENTS OF THE LOW-REYNOLDS-NUMBER FLOW AROUND AN SD7003 AIRFOIL

presented by

ALAN W. KATZ

has been accepted towards fulfillment of the requirements for the

M.S. degree in Mechanical Engineering

Major Professør's Signăture

Date

MSU is an Affirmative Action/Equal Opportunity Employer

LIBRARY Michigan State University

PLACE IN RETURN BOX to remove this checkout from your record. **TO AVOID FINES** return on or before date due. **MAY_BE RECALLED** with earlier due date if requested.

| DATE DUE | DATE DUE | DATE DUE |
|----------|----------|----------|
| | | |
| | | |
| | | |
| | | |
| | | |
| | | |
| | | |
| | | |
| | | |
| | | |

5/08 K:/Proj/Acc&Pres/CIRC/DateDue.indd

MOLECULAR TAGGING VELOCIMETRY MEASUREMENTS OF THE LOW-REYNOLDS-NUMBER FLOW AROUND AN SD7003 AIRFOIL

Ву

Alan W. Katz

A THESIS

Submitted to
Michigan State University
in partial fulfillment of the requirements
for the degree of

MASTER OF SCIENCE

Mechanical Engineering

2010

ABSTRACT

MOLECULAR TAGGING VELOCIMETRY MEASUREMENTS OF THE LOW-REYNOLDS-NUMBER FLOW AROUND AN SD7003 AIRFOIL

By

Alan Katz

In aerodynamics, the performance of a lifting surface depends upon the speed and length scale at which it operates. At low Reynolds numbers, flow on the suction surface of an airfoil may separate, leading to an open separation, or a closed laminar separation bubble (LSB). This flow condition has gained more attention recently due to its relevance to small unmanned aircrafts known as micro aerial vehicles (MAVs). In this work, molecular tagging velocimetry (MTV) experiments are performed on the suction surface of a Selig/Donovan 7003 airfoil model in a water tunnel at three Reynolds numbers (on the order of 10⁴) and a range of angles of attack. The MTV line-tagging method utilized measures the streamwise component of velocity at very fine spatial resolution, (0.03% of the chord length) in the cross-stream direction. The separation and reattachment locations are determined, and the mean and fluctuations of the stream-wise velocity are studied. These results are compared to those from previous PIV measurements and CFD simulations. Good agreement is displayed in the separation locations for all studies, while the reattachment locations range in disagreement from slight to significant. The influence of factors such as freestream turbulence, three-dimensional spanwise effects, and spatial resolution, which are suspected to affect the measured reattachment point, are discussed.

Copyright by ALAN WILLIAM KATZ 2010

ACKNOWLEDGEMENTS

I would first like to thank my advisors, Drs. Manoochehr Koochesfahani and Ahmed Naguib, for sharing the challenge of working on this project with me and giving me endless support and advice throughout the whole experience. I greatly appreciate their faith in allowing me to take on this project, which has been very challenging, very difficult, and very rewarding to take part in. I would also like to thank the Air Force Research Laboratory at Wright-Patterson Air Force Base for supporting this project. Many thanks to Mike Mclean of the engineering machine shop, who built and continually modified my test rig throughout the course of this project, and whose friendly demeanor and pleasant conversation made working with him a joy. I also would like to thank Dr. Doug Bohl, who helped guide me along with his expertise on the facilities I used.

A large number of thank-yous are due to my lab mates. Dr. Shahram Pouya offered seemingly endless wisdom in technical and administrative matters, and always made time to help me on any problem I encountered in the lab. Dr. Vibhav Durgesh was also a great resource, for both technical matters and a good laugh, and he is due credit for writing from scratch the processing code which I used. Thanks to Rohit for being a good friend, offering advice, and sharing almost daily with me an often very necessary coffee break. Thanks to Krishna for sharing in discussion with me on many topics, from lab issues to motorcycle riding. I would also like to thank David for arriving just in time to help me process all my data. Without his programming expertise I would have been in big trouble many times.

I would also like to thank my friends and especially my family for supporting me in many ways since I have begun this endeavor. Special thanks to my mom, Charlotte, my dad, Stephen, and sister, Erin.

TABLE OF CONTENTS

| LIST O | F TABLES | vii |
|--------|---|------|
| LIST O | F FIGURES | viii |
| LIST O | F SYMBOLS AND ABBREVIATIONS | xiii |
| 1. BA | CKGROUND AND MOTIVATION | 1 |
| 1.1. | LOW-REYNOLDS-NUMBER AIRFOILS | 1 |
| 1.2. | SELIG/DONOVAN 7003 AIRFOIL | 3 |
| 2. EX | PERIMENTAL FACILITY AND MEASUREMENT TECHNIQUES. | 6 |
| 2.1. | FACILITY | 6 |
| 2.1. | .1. TWO-FOOT CLOSED-LOOP WATER TUNNEL | 6 |
| 2.1. | .2. AIRFOIL | 19 |
| 2.2. | MOLECULAR TAGGING VELOCIMETRY TECHNIQUE | 22 |
| 2.2. | .1. METHOD BACKGROUND | |
| 2.2. | | 24 |
| 2.2 | 3. IMAGE ACQUISION | |
| | 4. ONE-COMPONENT PROCESSING | |
| 3. DA | TA AND RESULTS | |
| 3.1. | POST-PROCESSING AND ANGLE ISSUES | 35 |
| 3.2. | SEPARATION AND REATTACHMENT | 45 |
| 3.3. | MEAN AND FLUCTUATION VELOCITY DATA | |
| 3.4. | LITERATURE COMPARISON | 63 |
| 3.5. | FUTURE WORK | |
| APPEN | DIX | 81 |
| DEFED | FNCES | 02 |

LIST OF TABLES

| Table 1.1: Comparison of separation and reattachment locations obtained three experimental facilities and one CFD study on the SD7003 for $Re_c = 60,000$ and $\alpha = 4^{\circ}$. *Institute for Aerospace Research, [†] Technical University of Braunschweig, [‡] Air Force Research Laboratory. All experimental results are taken from Ol <i>et al.</i> [2005] and the numerical data is taken from Galbraith <i>et al.</i> [2008] | 5 |
|---|---|
| Table 2.1: Freestream angle calibration from two-component measurements. Note that the chord length is 200.95 mm and the kinematic viscosity is 0.0095 cm ² /s in all cases. | 8 |
| Table 2.2: Delays used between the MTV image pair at different Reynolds numbers. The delays were decreased as the freestream speed of the tunnel was increased to keep the displacement nominally at half the line spacing. Also given in the table is the gate (exposure) period for the undelayed and delayed images | 8 |
| Table 2.3: The effect of down sampling on the mean and RMS velocity in (a) the shear layer and (b) the freestream. The mean and RMS are presented with their percent difference from the original rate of 30 Hz. | 3 |
| Table 3.1: Discrepancies between the calibrated angles and those determined by a least-squares fit to the experimental profile. calibrated angles are those determined by the initial imaging-based calibration. The experimental data are the angles determined by the fit and the RMS error of the fit | 8 |
| Table 3.2: Simulation testing the robustness of the fitting routine used in the experiment. The mean of the noise was zero in all cases. The angle is recovered well within the accuracy of the fit, with the shorter and longer chord lines resulting in changes mostly in the horizontal offset used | 1 |
| Table 3.3: Initial calibration angles and corresponding fit-determined angles using the same images. These angles are relative to the reference line and therefore not the angle of attack. The reference line angle, chord line angle, and chord length are also shown to demonstrate consistency across the four calibrations. | 4 |
| Table 3.4: Separation and reattachment data for the cases investigated. A dash indicates that the flow did not reattach. Locations are normalized by the chord length. Uncertainty in separation and reattachment points is ± 0.0055 x/c | 1 |

LIST OF FIGURES

| Figure 1.1: The SD7003 shape. The chord line and angle of attack are shown | 4 |
|--|----|
| Figure 2.1: Schematic view of the 10,000 liter closed loop water tunnel. Original schematic by Drs. C. Gendrich and D. Bohl. | 7 |
| Figure 2.2: Optical arrangement for UV laser beam | 8 |
| Figure 2.3: Time series of freestream flow at a point. | 10 |
| Figure 2.4: Filtered time series. This is the same time series as shown in Figure 2.3 after filtering with 41-point moving average. | 11 |
| Figure 2.5: Time series acquired in the shear layer in the flow around the airfoil, and freestream, acquired at the same time. | 12 |
| Figure 2.6: RMS convergence in the shear layer. The dotted line shows the trend of narrowing data scatter as sampling time is increased | 14 |
| Figure 2.7: Convergence results for mean and RMS in the shear layer and freestream. | 15 |
| Figure 2.8: Coordinate system and freestream angle sign convention. | 16 |
| Figure 2.9: Two-component UV optics set-up for quantifying freestream angle. The beam-splitter allows the creation of two beams that can then be broken into lines that intersect to create a grid | 17 |
| Figure 2.10: Measured suction-side surface points and corresponding difference error | 20 |
| Figure 2.11: Airfoil rig | 21 |
| Figure 2.12: A typical MTV image pair is shown, along with the corresponding vector field determined by the pair. (a) The undelayed image is taken 1µs after excitation. (b) The tagged grid is shown after 8 ms. (c) The resultant vector field found from (a) and (b). [Gendrich et al., 1997] | 23 |
| Figure 2.13: Example of a one-component MTV image pair. $\alpha = 6^{\circ}$, Re=20,000, $x \approx c/3$. (a) The undelayed image is shown 2 μ s after the laser pulse. (b) The delayed image, taken 10 ms later, shows the instantaneous streamwise velocity profile. | 25 |
| PIVIIIV | 2 |

| Figure 2.14: Camera timing diagram. The Fsync signal is the internal clock of the CCD chip, which is used as a reference to create the other timing signals. The undelayed image is taken 2 µs after the laser pulse to avoid fluorescence emission. The delay is defined as the center-to-center distance between the undelayed and delayed gate periods. The widths of the Fsync pulses are ~0.8 ms; this corresponds to the time needed to send the image data from the camera to the acquisition system. |
|--|
| Figure 2.15: Ten overlapping fields of view (alternating blue and red) required to capture all the velocity at the surface of the airfoil |
| Figure 2.16: Undelayed and delayed intensity profiles, taken from the middle of the fifth line from the left in the images in Figure 2.13. All the other lines' intensities are masked out and replaced by a constant background value |
| Figure 2.17: (a) Complete correlation coefficient for the profiles shown in Figure 2.16. (b) Detailed view of the 7 th order polynomial fit to the peak for subpixel accuracy. |
| Figure 3.1: An average of undelayed images shows bright spots near the surface36 |
| Figure 3.2: Matched theoretical profile with simulated experimental profile for RMS _{noise} = 4 pixels, mean _{noise} = 10 pixels |
| Figure 3.3: Processed calibration image for use in determining the angle of attack for the 8 degree case (inverted contrast). The edge detection was unable to pick up the trailing edge |
| Figure 3.4: Unreliable mean velocity vectors near the surface increase, instead of continuing to smoothly approach zero at the wall. From Re = $20,000$ and $\alpha = 3.75^{\circ}$ case. |
| Figure 3.5: Example of bad vector replacement routine. The fit is applied before scaling the raw pixel displacement data. The green experimental data are shown to demonstrate the shape of the profile. The blue experimental data are used for the fit. The black data are bad vectors that have been skipped and replaced. All red data (10 points) are from the curve fit, with the triangular point as a "link" between the bad data and the good data to make the profile smooth. |

| Figure 3.6: Velocity profile from Figure 3.4 after curve fitting is applied. The last seven vectors nearest to the surface were determined to be unreliable, and an additional vector above that was used as a "link" between the real and curve fit data to make the profile smooth, for a total of eight vectors being replaced by curve fit data. | .48 |
|--|-----|
| Figure 3.7: Mean velocity profiles, between which separation occurs, overlaid on a mean velocity contour map. The units of the velocity contour "color scale" (displayed on the right) are mm/s. Re = $20,000$ and $\alpha = 7.3^{\circ}$ case | .49 |
| Figure 3.8: Mean velocity profiles near the reattachment point, overlaid on a velocity contour map. The units of the velocity contour "color scale" (displayed on the right) are mm/s. Every other vector is plotted in the cross-normal direction. Re = $40,000$ and $\alpha = 5.49^{\circ}$ case. | .50 |
| Figure 3.9: Separation and reattachment data plots for $Re = 20,000$ and $Re = 30,000$ for all measured angles. | .52 |
| Figure 3.10: Separation and reattachment data for $Re = 40,000$ | .55 |
| Figure 3.11: Separation, reattachment, and bubble length as a function of Reynolds number for $\alpha \approx 7.3^{\circ}$ | .56 |
| Figure 3.12: Evolution of normalized mean velocity U (U/U_{∞}) as a function of angle of attack for a Reynolds number of 40,000 | .57 |
| Figure 3.13: Evolution of fluctuations $((u'/U_{\infty})^2)$ as a function of angle of attack for a Reynolds number of 40,000. | .58 |
| Figure 3.14: Average of 50 delayed images from the $\alpha = 10.44^{\circ}$ Re = 40,000 case. Intensities are extracted along the white line for display in Figure 3.15 | .59 |
| Figure 3.15: Intensity profile extracted along the white line from Figure 3.14 to highlight the close proximity of the peaks. Peaks as close as this can produce erroneous correlations in the processing technique. | .60 |

| Figure 3.16: Mean <i>u</i> -component velocity (U/U_{∞}) evolution with Reynolds number at a nominal angle of attack of 3.5°. | .61 |
|---|-----|
| Figure 3.17: Evolution of normalized fluctuations of u $((u''U_{\infty})^2)$ with Reynolds number at a nominal angle of attack of 3.5°. | .63 |
| Figure 3.18: Separation and reattachment locations: Comparison between MTV (TMUAL) measurements and PIV [Burgmann et al., 2008] measurements at a Reynolds number of 20,000. | .65 |
| Figure 3.19: Effect of turbulence intensity on separation and reattachment points in PIV measurements. [Burgmann <i>et al.</i> , 2007, 2008] | .67 |
| Figure 3.20: Separation and reattachment comparison between MTV (TMUAL) measurements and PIV [Burgmann <i>et al.</i> , 2008] measurements at a Reynolds number of 40,000. | .70 |
| Figure 3.21: Separation point as a function of angle of attack for three Reynolds numbers. | .71 |
| Figure 3.22: Reattachment point as a function of angle of attack for three Reynolds numbers | .72 |
| Figure 3.23: Comparison of quadratic and linear models for interpolating TMUAL data. Separation and reattachment are shown for a Reynolds number of 40,000 | .73 |
| Figure 3.24: Comparison of TMUAL (interpolated) and ILES [Galbraith <i>et al.</i> , 2008] separation and reattachment data at an angle of attack of 8° as a function of Reynolds number. | .74 |
| Figure 3.25: Normalized mean streamwise velocity (U/U_{∞}) contour from TMUAL data, and normalized mean u contour (in airfoil coordinates) from CFD data. | .77 |

| Figure 3.26: Fluctuation $((u'/U_{\infty})^2)$ contours from TMUAL and CFD data78 |
|---|
| Figure A.1: (a) Normalized mean (U/U_{∞}) and (b) fluctuation $((u'/U_{\infty})^2)$ of streamwise velocity component for $\alpha = 3.75^{\circ}$ and $Re = 20,00082$ |
| Figure A.2: (a) Normalized mean (U/U_{∞}) and (b) fluctuation $((u'/U_{\infty})^2)$ of streamwise velocity component for $\alpha = 5.65^{\circ}$ and $Re = 20,000$ |
| Figure A.3: (a) Normalized mean (U/U_{∞}) and (b) fluctuation $((u'/U_{\infty})^2)$ of streamwise velocity component for $\alpha = 7.30^{\circ}$ and $Re = 20,00084$ |
| Figure A.4: (a) Normalized mean (U/U_x) and (b) fluctuation $((u'/U_x)^2)$ of streamwise velocity component for $\alpha = 10.55^{\circ}$ and $Re = 20,00085$ |
| Figure A.5: (a) Normalized mean (U/U_{∞}) and (b) fluctuation $((u'/U_{\infty})^2)$ of streamwise velocity component for $\alpha = 3.49^{\circ}$ and $Re = 30,000$ |
| Figure A.6: (a) Normalized mean (U/U_x) and (b) fluctuation $((u'/U_x)^2)$ of streamwise velocity component for $\alpha = 7.39^{\circ}$ and $Re = 30,000$ |
| Figure A.7: (a) Normalized mean (U/U_x) and (b) fluctuation $((u'/U_x)^2)$ of streamwise velocity component for $\alpha = 3.59^{\circ}$ and $Re = 40,000$ 88 |
| Figure A.8: (a) Normalized mean (U/U_x) and (b) fluctuation $((u'/U_x)^2)$ of streamwise velocity component for $\alpha = 5.49^{\circ}$ and $Re = 40,00089$ |
| Figure A.9: (a) Normalized mean (U/U_x) and (b) fluctuation $((u'/U_x)^2)$ of streamwise velocity component for $\alpha = 7.29^{\circ}$ and $Re = 40,00090$ |
| Figure A.10: (a) Normalized mean (U/U_{∞}) and (b) fluctuation $((u'/U_{\infty})^2)$ of streamwise velocity component for $\alpha = 10.44^{\circ}$ and $Re = 40,00091$ |

LIST OF SYMBOLS AND ABBREVIATIONS

c Airfoil chord length

CCD Charge coupled device

 $f_{\rm s}$ Sampling frequency

LSB Laminar separation bubble

MAV Micro Aerial Vehicle

MTV Molecular Tagging Velocimetry

Re Reynolds number

Re_c Reynolds number based on chord length

RMS Root mean squared deviation

 U_{∞} Freestream velocity

u,v,w Instantaneous velocity components in tunnel coordinate system

U,V,W Mean velocity components in tunnel coordinate system

u',v',w' Velocity component fluctuations in tunnel coordinate system

UAV Unmanned Aerial Vehicle

x,y,z Airfoil coordinate system

x',y',z' Tunnel coordinate system

α Airfoil angle of attack

Δt Image delay period

μ Fluid dynamic viscosity

v Fluid kinematic viscosity

ρ Fluid density

1. BACKGROUND AND MOTIVATION

It has long been known in the field of aerodynamics that the performance of a lifting surface is dependent on the speed and length scale at which it operates. This phenomena is known as scale effect [Lissaman, 1983], and its implications range from the flight of an insect to that of a jumbo-jet. At low speeds and physical scales, interesting phenomena occur in the flow around airfoils. In this work, some of the features of this type of flow around a specific airfoil are measured and studied. In these introductory sections, these flow phenomena, their causes, and their impacts are reviewed.

1.1. LOW-REYNOLDS-NUMBER AIRFOILS

In many flows, a critical parameter is the Reynolds number (Re). The Reynolds number is the ratio of the inertial forces to the viscous forces present in a flow. In general, Re is defined by Equation (1).

$$Re = \frac{\rho UL}{\mu} \tag{1}$$

Where ρ is the density of the fluid, μ is the dynamic viscosity of the fluid, U is a characteristic velocity, and L is a characteristic length of the flow. In this work, an airfoil is being studied, and therefore the Reynolds number based on the airfoil chord, denoted by Re_c , is defined in Equation (2).

$$Re_c = \frac{\rho U_{\chi} c}{\mu}$$
 (2)

In Equation (2), the characteristic velocity is the freestream velocity U_{∞} , and the characteristic length is the chord of the airfoil c. The chord length is defined as the distance from the leading edge (front) to the trailing edge (rear) of the airfoil (see Figure 1.1). Because this entire work is based on measurements made on an airfoil, the chord-based Reynolds number will hereafter be referred to merely as Reynolds number.

When discussing most airfoil flows, the focus is usually based on the assumption that the Reynolds number is on the order of 10^7 - 10^8 , the range in which most general aviation and large aircraft operate [Lissaman, 1983]. In this Reynolds number range, the flow over the airfoil remains attached for most angles of attack (α , see Figure 1.1). This is because the Reynolds number is sufficiently high so as to cause transition of the boundary layer to turbulence. The turbulent boundary layer offers resistance to separation due to the added momentum caused by the enhanced turbulence. As the angle of attack is increased, lift also is increased, until a critical angle is reached at which the flow separates near the leading edge due to the strong adverse pressure gradient present. This flow condition is known as stall, which causes decreased lift and loss of control. Stall is therefore avoided in practical applications.

At lower Reynolds numbers, ranging from 10⁴-10⁵, a very different flow structure is present. Instead of transitioning to turbulent state, the boundary layer remains laminar, and therefore, is more susceptible to separation, even at low angles of attack. The separation generally occurs near the leading edge, and the resulting shear layer then

rapidly transitions to turbulence, reattaching to the airfoil surface in some cases. When the flow reattaches, a closed structure known as a laminar separation bubble (LSB) is formed, and when high enough angle of attack is reached, the bubble can burst and remain open. Because of the instability of the separated shear layer that is formed, transition to turbulence is often observed after separation. When this occurs, the LSB is highly unsteady in nature, and therefore provides a challenging problem to study.

In recent years, the study of aerodynamics in the Reynolds number range from 10^4 - 10^5 has garnered greater attention because of its relevance to the flight of unmanned aerial vehicles (UAVs), including especially a subset of UAVs known as micro aerial vehicles (MAVs) [Galbraith *et al.*, 2008]. MAVs typically operate in the range of $Re_c \approx 10^4$, so it is apparent that flow separation, and in some cases, an LSB is present. The structure and unsteadiness of separation and the LSB have a negative impact on the performance and control of MAVs. It is therefore beneficial to the further development of these aircrafts to study the behavior of the flow at these low Reynolds numbers.

1.2. SELIG/DONOVAN 7003 AIRFOIL

In this work, the airfoil model that is studied is the Selig/Donovan (SD) 7003 airfoil. This airfoil is chosen because of its widespread use in both CFD [Galbraith *et al.*, 2008] and PIV [Burgmann *et al.*, 2007,2008, and Ol *et al*, 2005] studies which are also focused on low-Reynolds-number airfoil flows. The SD7003 is often studied because flow separation often occurs, even at very low angles of attack.

The SD7003 is a cambered airfoil, the coordinates for which are available from the UIUC Airfoil Coordinates Database [Selig]. The coordinates are plotted in Figure 1.1, showing the shape of the airfoil. The chord line, which connects the leading edge and trailing edge of the airfoil, is also shown, as well as the angle of attack, which is the angle between the chord line and the freestream flow direction.

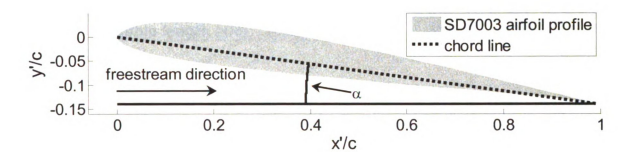


Figure 1.1: The SD7003 shape. The chord line and angle of attack are shown.

Previously, PIV measurements and CFD simulations have been performed on this airfoil shape to study the open separation and LSB. A major issue in this research is that the results obtained using these two different approaches generally do not agree well. Even comparing the experimental results amongst themselves shows marked disagreement. In the work by Ol et al. [2005], results from three different experimental facilities, all utilizing PIV, showed that though the velocity fields and LSB shape were consistent, the locations of separation and reattachment were very different.

shows separation and reattachment data for three experiments and one set of computations to highlight the clear differences that can be present across techniques. It is posited that these differences could be due to the different aspect ratios of the airfoil

models used in the experiments, freestream turbulence level of the flow facilities, and the resolution of the measurements or simulation.

Table 1.1: Comparison of separation and reattachment locations obtained three experimental facilities and one CFD study on the SD7003 for $Re_c = 60,000$ and $\alpha = 4^{\circ}$. *Institute for Aerospace Research, [†]Technical University of Braunschweig, [‡]Air Force Research Laboratory. All experimental results are taken from Ol *et al.* [2005] and the numerical data is taken from Galbraith *et al.* [2008].

| | IAR* | TU-BST | AFRL+ | ILES ³ |
|---------------------|-------|--------|-------|-------------------|
| Separation (x/c) | 0.330 | 0.300 | 0.180 | 0.230 |
| Reattachment (x/c) | 0.630 | 0.620 | 0.580 | 0.650 |
| Bubble length (x/c) | 0.300 | 0.320 | 0.400 | 0.420 |

In this work, molecular line-tagging velocimetry experiments are performed on an SD7003 airfoil model in a water tunnel. These experiments allow comparison of the separation and reattachment positions to previous studies that utilized PIV and CFD. By using a molecular line-tagging method to make measurements, the streamwise velocity component (u) is extracted at very fine spatial resolution in the direction normal to freestream, allowing for detection of the flow separation and reattachment. From the one-component data, mean (U) and fluctuation (u') quantities are determined and compared with the results of the previous works.

2. EXPERIMENTAL FACILITY AND MEASUREMENT TECHNIQUES

In this work, a set of facilities, techniques, and instrumentation are combined to gather and process data. It is therefore prudent to review in detail the equipment and methods used to show how they were combined for these experiments. Images in this thesis are presented in color.

2.1. FACILITY

2.1.1. TWO-FOOT CLOSED-LOOP WATER TUNNEL

The flow facility in this study is a 10,000 liter closed-loop water tunnel used to create the oncoming flow to the airfoil, built by Engineering Laboratory Design. The water tunnel is located in the Turbulent Mixing and Unsteady Aerodynamics Laboratory (TMUAL) at Michigan State University (MSU) in East Lansing, Michigan. The test section has a 61 x 61 cm (2' × 2') cross section and 244 cm (8') length, and is constructed of scratch-resistant Plexiglass, which allows optical access from beneath and both sides. The top of the test section is open, leaving a free surface. In this work, all image collection was completed from one side, with the freestream flow traveling from left to right from the perspective of the camera. Figure 2.1 contains a schematic of the water tunnel and flow management devices.

Flow management in the tunnel included two perforated stainless steel baffles (plates), a honeycomb, and fine screen upstream of the contraction section, as shown in Figure 2.1. Additional flow management was included (as shown) at the most upstream end of the test section, and included a honeycomb and fine screen.

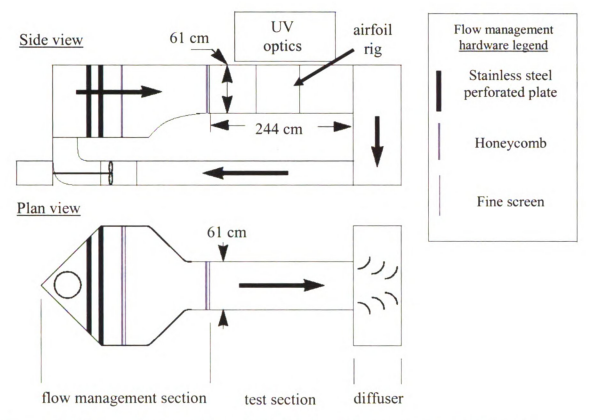


Figure 2.1: Schematic view of the 10,000 liter closed loop water tunnel. Original schematic by Drs. C. Gendrich and D. Bohl.

In order to utilize the one-component molecular tagging velocimetry (MTV) technique (see section 2.2.2), a UV laser beam was redirected by a series of UV-reflective mirrors through the free surface of the tunnel. The beam cannot be sent through the Plexiglass sides of the test section since they are not transmissive for UV wavelengths. The beam was then focused by a variable focal length (VFL) system into a thin sheet which is less than 1 mm thick at the measurement location. The VFL is composed of two cylindrical lenses in series, whose relative position can be varied, changing the focal length of the lens system. To create individual tagged lines, a slotted brass plate was placed in the path

of the laser sheet just before entering the water and tracer mixture in the tunnel. Because the beam was sent through the free surface, any surface features (such as waves, bubbles, or other disturbances) could have altered the shape and direction of the focused beam. To ensure the beam is not affected by the fluid surface, a beam management window (BMW) was used. The BMW is a $10 \times 5 \times \frac{3}{4}$ inch Plexiglass sheet with rounded edges that sits half-submerged in the free surface of the water. The edges are rounded to prevent any interference with the freestream flow in the test section. In the center of the BMW is a quartz window, one inch wide and seven inches long, which allows the UV laser sheet to pass through with minimal losses. This UV optics set-up is shown schematically in Figure 2.2.

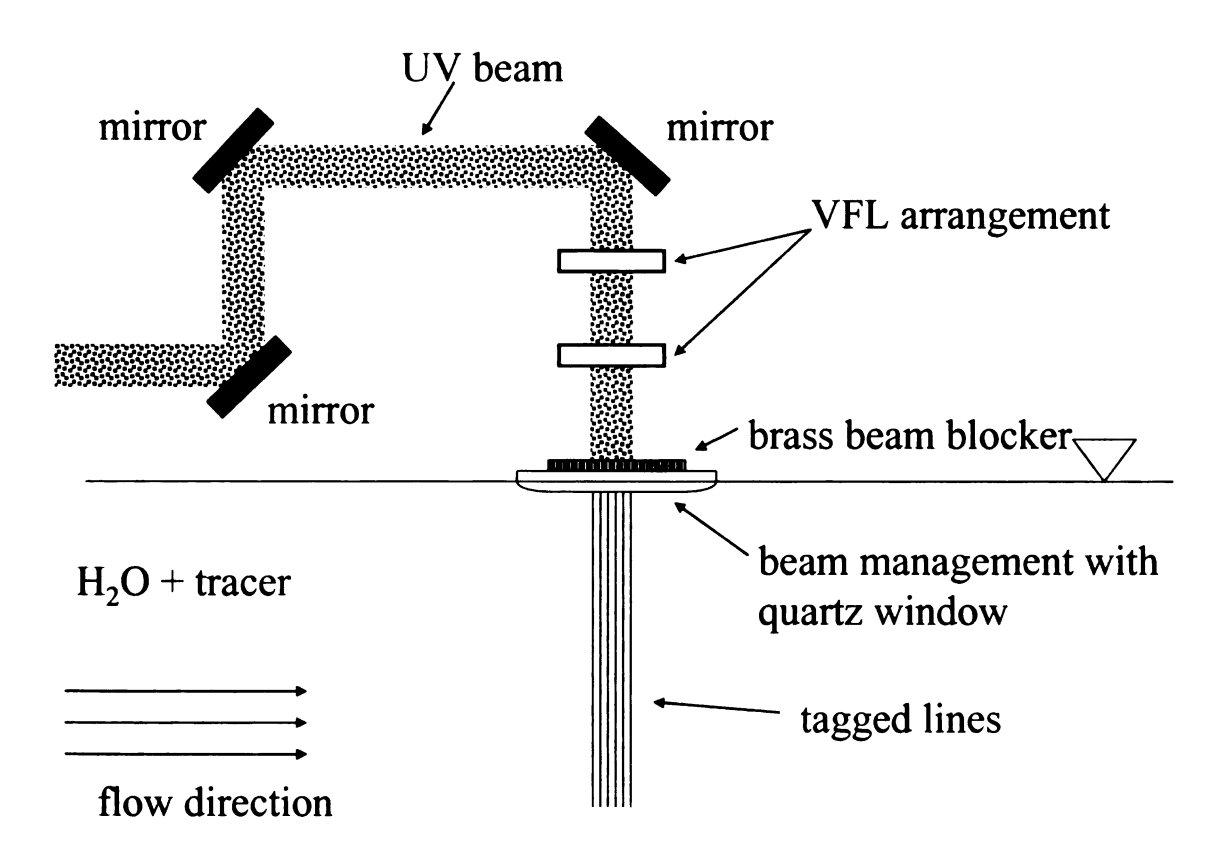


Figure 2.2: Optical arrangement for UV laser beam

Before any measurements could be made on the airfoil, the freestream flow of the tunnel was studied. Characterization of the freestream can be divided into two categories: freestream fluctuations and freestream angles.

The freestream flow in the water tunnel used in this study was characterized by low frequency velocity fluctuation. It is speculated that this is caused by a "U-tube" oscillation effect. This low frequency component is observed in Figure 2.3, along with high frequency fluctuations. The fluctuation (root mean square of the deviation from the mean, hereafter referred to as simply RMS) of this signal is 2.8% of the mean, which includes all the flow fluctuations (low and high frequency) and noise from imaging and data processing. The low and high frequency components of fluctuation, regardless of their source, are related by Equation (3) to the total measured fluctuation level measured.

$$u_{total}^{\prime 2} = u_{high}^{\prime 2} + u_{low}^{\prime 2} \tag{3}$$

To determine what component of the RMS figure is due to the low frequency flow RMS (u'_{low} in Equation (3)), the same time series was filtered with a 41-point moving average. The filtered signal is shown in Figure 2.4. It is apparent from inspection that in the filtered signal, most of the high frequency noise is removed. The RMS of the signal after filtering is $u'_{low} = 2.11\%$. By plugging this into Equation (3), it is found that the low frequency component makes up 57% of the fluctuations in the measurement, while the other 43% is made up by high frequency fluctuations. The low frequency fluctuations

contribute significantly to the turbulence level I (also called turbulence intensity, freestream turbulence, etc.) in the tunnel, as defined in Equation (4).

$$I = \frac{u'_{total}}{U_{\infty}} \tag{4}$$

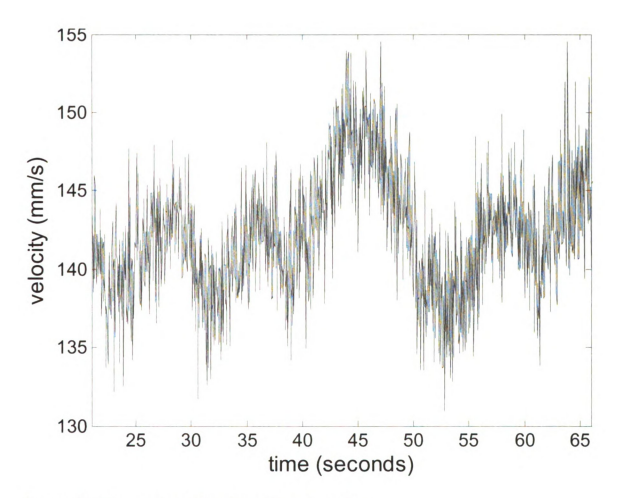


Figure 2.3: Time series of freestream flow at a point.

It was also observed in early experiments that there was a low frequency variation in the flow around the airfoil. This was first noticed during a visualization of the separated shear layer above the suction surface, in which it appeared that the shear layer was slowly moving up and down. To better understand this process and to see how the fluctuations in the freestream affect the shear layer, data were acquired far enough above the airfoil to reach nearly into the freestream flow, while still capturing data in the shear layer. In this way, it was possible to acquire data about both fluctuations simultaneously. The time series of both are plotted on the same axes in Figure 2.5.

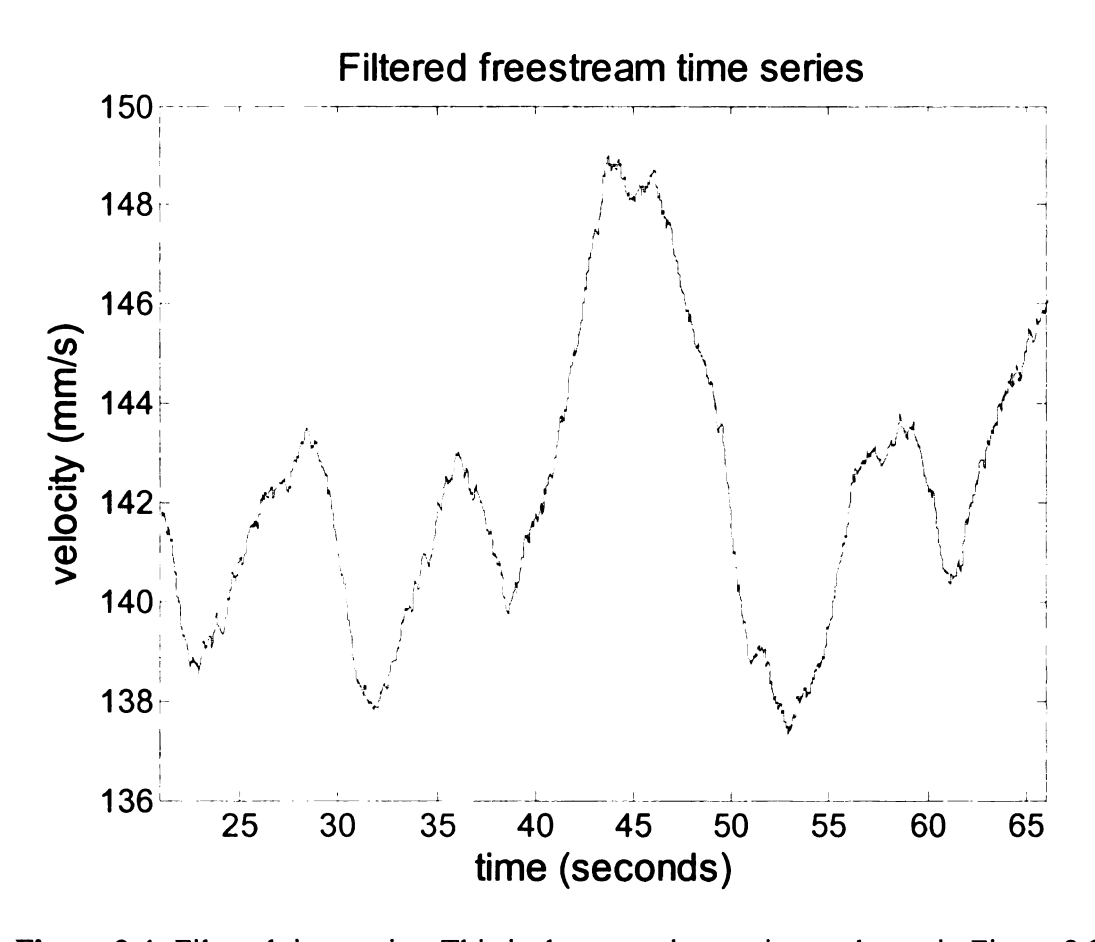


Figure 2.4: Filtered time series. This is the same time series as shown in Figure 2.3 after filtering with 41-point moving average.

From visual inspection, it is obvious both flows display low frequency characteristics, though the amplitude is much higher in the shear layer, where large velocity gradients exist. The period of each appears to be on the order of ~20 s, and indeed, frequency spectra analysis yields peaks at a 0.05 Hz. Because statistics of low frequency events such as these require sampling times that include many cycles, it was necessary to determine the acquisition time for each data set that would be needed to allow the freestream fluctuations, as well as the shear layer fluctuations, to converge within an acceptable tolerance.

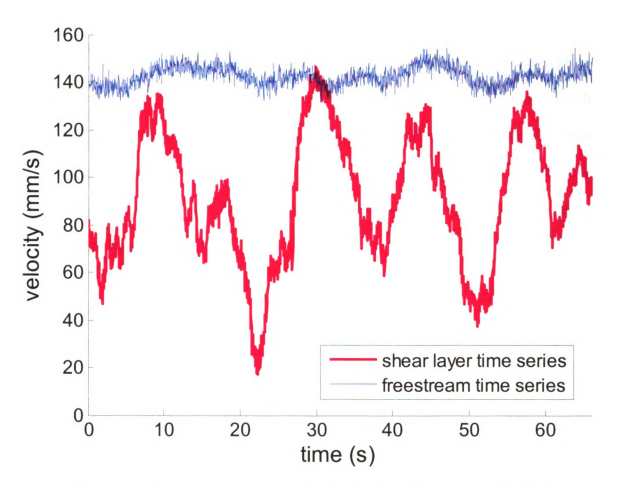


Figure 2.5: Time series acquired in the shear layer in the flow around the airfoil, and freestream, acquired at the same time.

To determine the convergence of the data, velocity data from a single field of view that included both the shear layer and near the "freestream" were used as mentioned above. Data were taken in 30 independent records, each with sampling time of 33 seconds. To begin, the statistics are found for each record separately, resulting in 30 different mean and RMS values for both the shear layer and freestream. These 30 mean and RMS values have their some variation because of the finite sample time of 33 s. The next step is to again calculate the statistics, this time taking two records together as a single record, doubling the sampling time to 66 seconds (but decreasing the number of available records by one half). The statistics are calculated and this process is repeated for sampling times of 166, 200, 333, and 500 seconds (6 records, 5 records, 3 records, and 2 records respectively). An exemplary plot of the effect of this statistical process is shown in Figure 2.6. This plot shows the narrowing of the spread as sampling time is increased for the RMS in the shear layer. The RMS is selected here for presentation because it is more sensitive to the record length than the mean. Large improvements in the scatter of the statistics are seen over the first few increases in sampling time, but the rate of improvement levels off quickly.

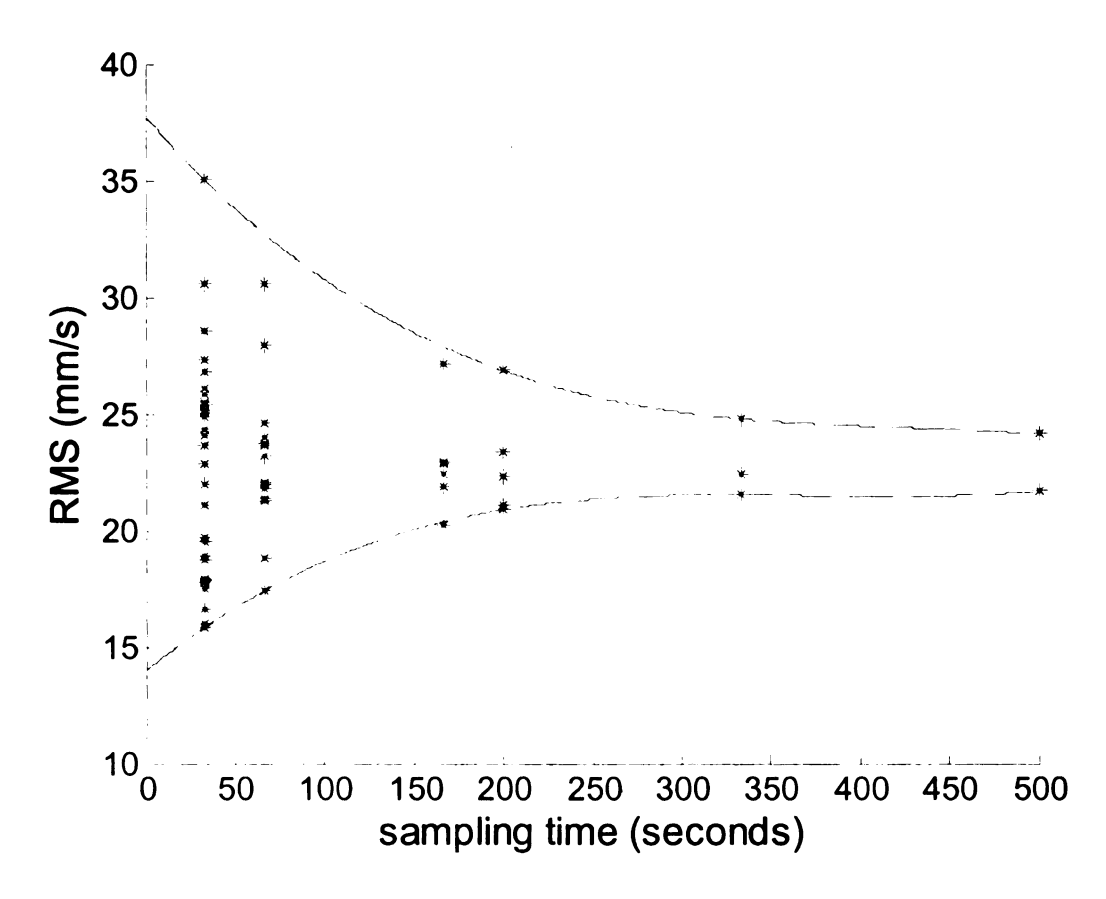


Figure 2.6: RMS convergence in the shear layer. The dotted line shows the trend of narrowing data scatter as sampling time is increased.

To quantify the convergence accuracy of the data, the RMS characterizing the variation in the statistical quantity is obtained. The effect of sampling time is compared for all the quantities in Figure 2.7 by plotting the percentage (of the mean of the given quantity) RMS as a function of sampling time. In examining this figure, it is apparent that the convergence quickly levels off after a sharp improvement. Due to time intensive data processing (see section 2.2.4), the high number of fields of view that are required for each experiment, and the marginal advantage in convergence that is achieved with longer sampling records, 150 s was chosen as the sampling time in these experiments.

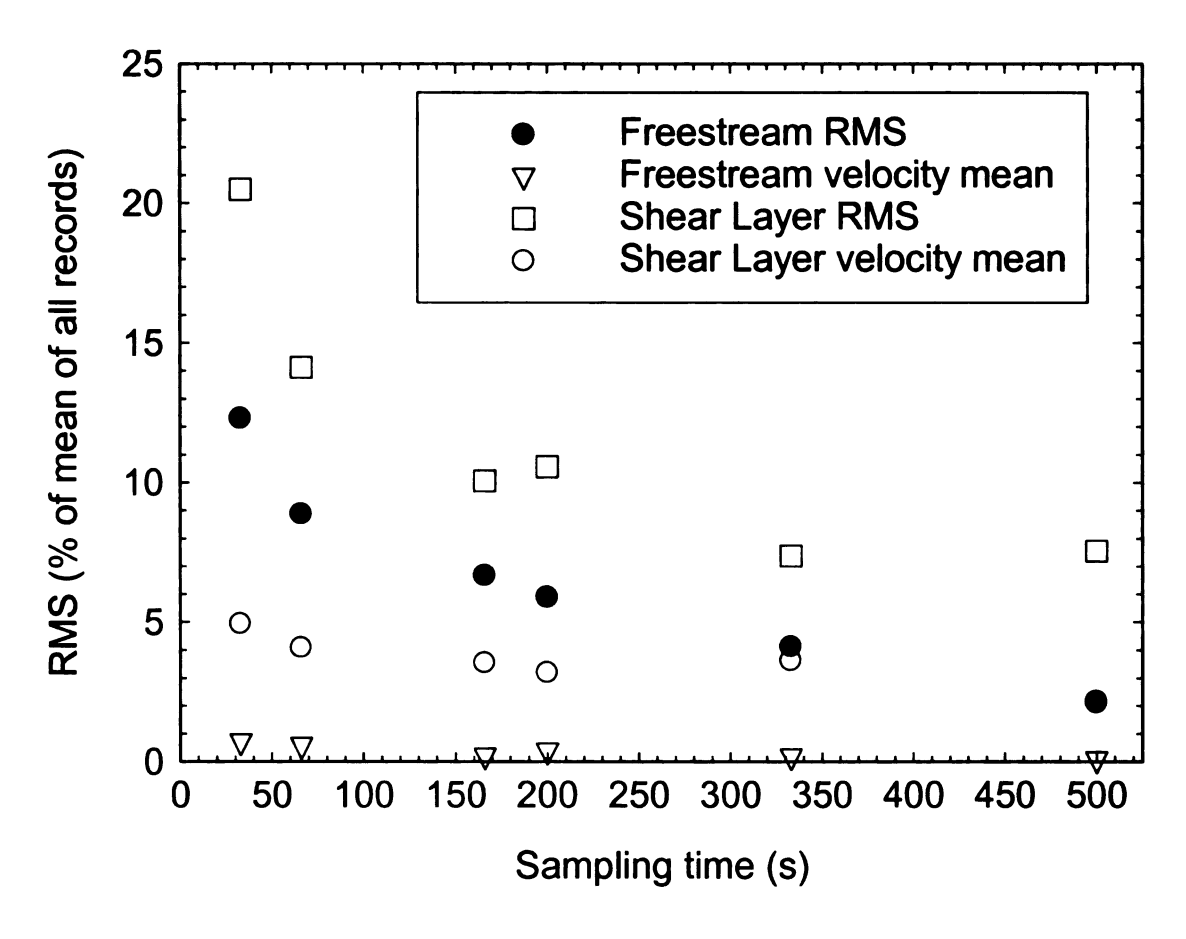


Figure 2.7: Convergence results for mean and RMS in the shear layer and freestream.

The next step in characterizing the flow in the tunnel is determining the freestream angle. Boundary layer growth on the bottom of the tunnel creates a slightly "upward" (toward the free surface) angle of the freestream flow. This means that though it is assumed the freestream flow is completely uniform and parallel to the tunnel (u-component only), there is a small v-component as well. The higher the growth rate of the boundary layer on the test section walls, the steeper the angle will be. Figure 2.8 shows the coordinate system and the sign convention used for the freestream angle for clarity. The primed coordinate system is aligned with the camera and bottom of the tunnel, and the unprimed

system (not shown) is a translation and rotation of the primed system such that the origin is at the leading edge of the airfoil, with the x-axis along the chord line of the airfoil. The reason for this coordinate transformation is described in more detail in section 3.1.

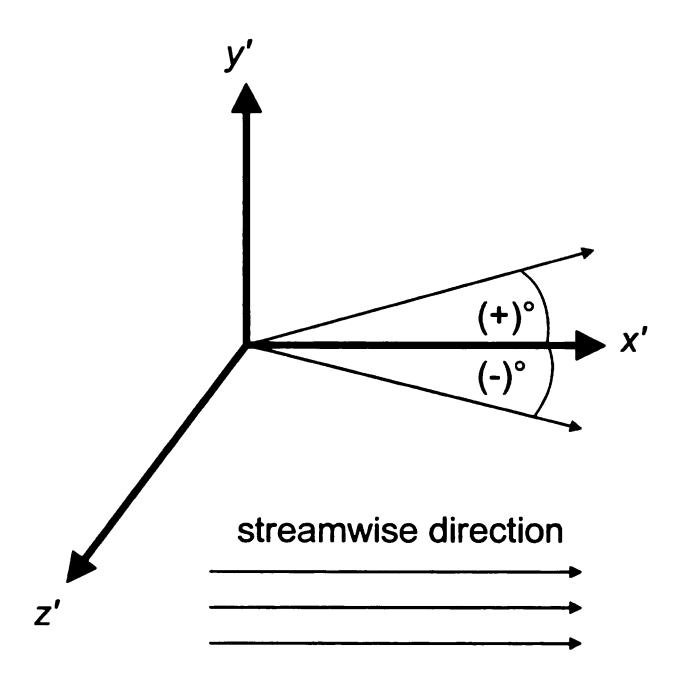


Figure 2.8: Coordinate system and freestream angle sign convention.

In order to quantify the freestream angle, two-component measurements were necessary. Because two-component measurements have been performed extensively in the TMUAL for many years, a fast, robust two-component processing program was available for use in these experiments. Thus, the main task in setting up this type of measurement was changing the UV optics to create a laser grid from two sheets, rather than lines from a single sheet. By adding a beam-splitter (50% reflection, 50% transmission) and two mirrors to the set-up shown in Figure 2.2, a grid was created upstream of the airfoil, shown schematically in Figure 2.9.

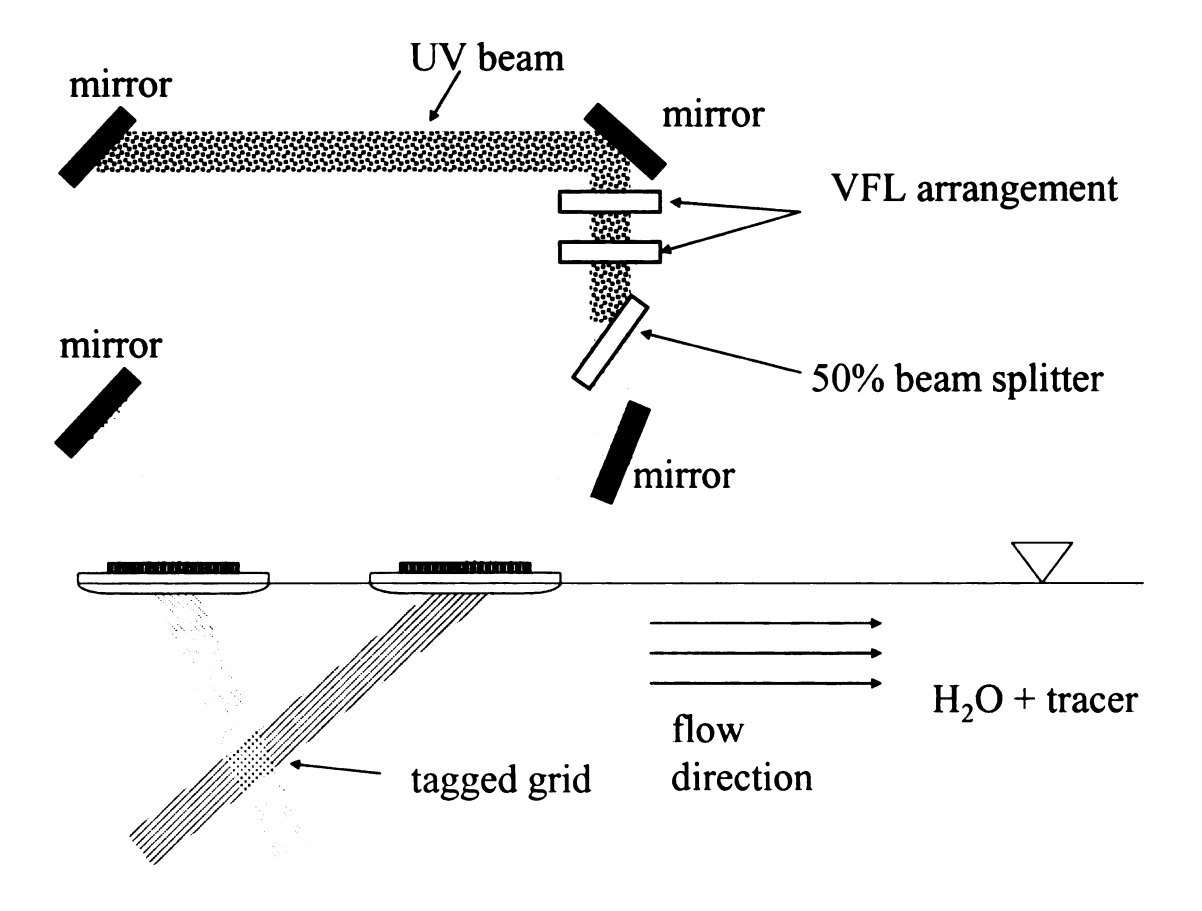


Figure 2.9: Two-component UV optics set-up for quantifying freestream angle. The beam-splitter allows the creation of two beams that can then be broken into lines that intersect to create a grid.

This particular configuration was very useful because it could be added to and removed from the tunnel without altering the one-component optics set-up. An additional camera was available and was fixed to collect the two-component data, thus the camera for the one-component measurements also didn't have to be disturbed to make upstream measurements. The data were collected two chord lengths upstream of where the airfoil would be placed, at the same height as the quarter-chord point of the airfoil. From the u and v (cross-stream velocity component) data, an angle was calculated for the three

speeds. The same data set was used to calibrate the freestream velocity against the pump controller setting, and calculate the Reynolds number. The results from this experiment are shown in Table 2.1. Note that hereafter, the Reynolds numbers quoted in this table will be referred to by the nearest factor of 10⁴ for simplicity. For example, the Reynolds number of 31,500 in the experiments will be referred to as 30,000.

Table 2.1: Freestream angle calibration from two-component measurements. Note that the chord length is 200.95 mm and the kinematic viscosity is 0.0095 cm²/s in all cases.

| u (mm/s) | u uncertainty (mm/s) | Rec | Re _c uncertainty | angle (°) |
|-------------|----------------------------|--------|-----------------------------|-----------|
| 99.5 | ± 2.8 | 21,000 | ± 590 | 0.26 |
| 148.8 | ± 3.6 | 31,500 | ± 760 | 0.14 |
| 197.2 | ± 4.7 | 41,700 | ± 990 | 0.14 |

With the freestream angles known, the angle of attack can be found by adding the freestream angle to the airfoil angle referenced to the bottom of the tunnel (see section 2.1.2 for details), which was determined with uncertainty of $\pm 0.4^{\circ}$. Because all the freestream angles found were within this uncertainty, an average of 0.2° was used for all freestream speed to factor into the angle of attack. Since the airfoil angle is referenced to the bottom of the tunnel, and the freestream angle is positive, the effect is a net increase of the angle of attack. That is, if the airfoil is set to 5.8° referenced to the bottom of the tunnel, then the actual angle of attack will be 6.0°. This is factored into the initial calibration described in section 2.1.2.

18

2.1.2. AIRFOIL

As discussed in Chapter 1, the airfoil used in this study is the Selig/Donovan (SD) 7003 low-Reynolds-number airfoil. The airfoil model in the present experiments has a nominal chord length of 20 cm (8 in.) and a nominal span of 45 cm (18 in.) with fiberglass construction, on loan from the Air Force Research Laboratory (AFRL). Upon receipt from the AFRL, it was observed that some holes were present on the surface and various dye-injection tubes were embedded in the airfoil. In addition to these tubes and holes, there were large gaps in the mid-span area of the model where struts were attached to pitch and plunge the airfoil during experiments. To prevent these surface features from affecting the flow of the airfoil, the tubes were removed and all the holes were filled with West System Marine Epoxy for boats. This material was chosen for its inert nature, waterproof seal, and resistance to the chemicals composing the phosphorescent tracer in the tunnel. The entire airfoil was covered in at least one layer of the epoxy so that the finish was consistent across the entire surface.

Due to the features on the airfoil and the subsequent alterations to the model, changes to the surface of the airfoil could have occurred. Because of the large modifications to the airfoil at the mid-span region to fill the spaces where the struts were connected, a spanwise location was chosen 45 mm (1.75 in.) off-center for making the measurements. To quantify how well the model matched the theoretical profile at this point, the suction surface of the airfoil model was measured at the span-wise plane where the MTV measurements were made. The height of the surface was measured, starting at the trailing edge, every 1 cm along the chord direction by a profiling probe attached to a milling

machine. A least-squares fit of the theoretical SD7003 shape to the measured profile is plotted in Figure 2.10, as well as the corresponding disagreement for each measured point. This least-squares fit was used in determining the chord length of the airfoil.

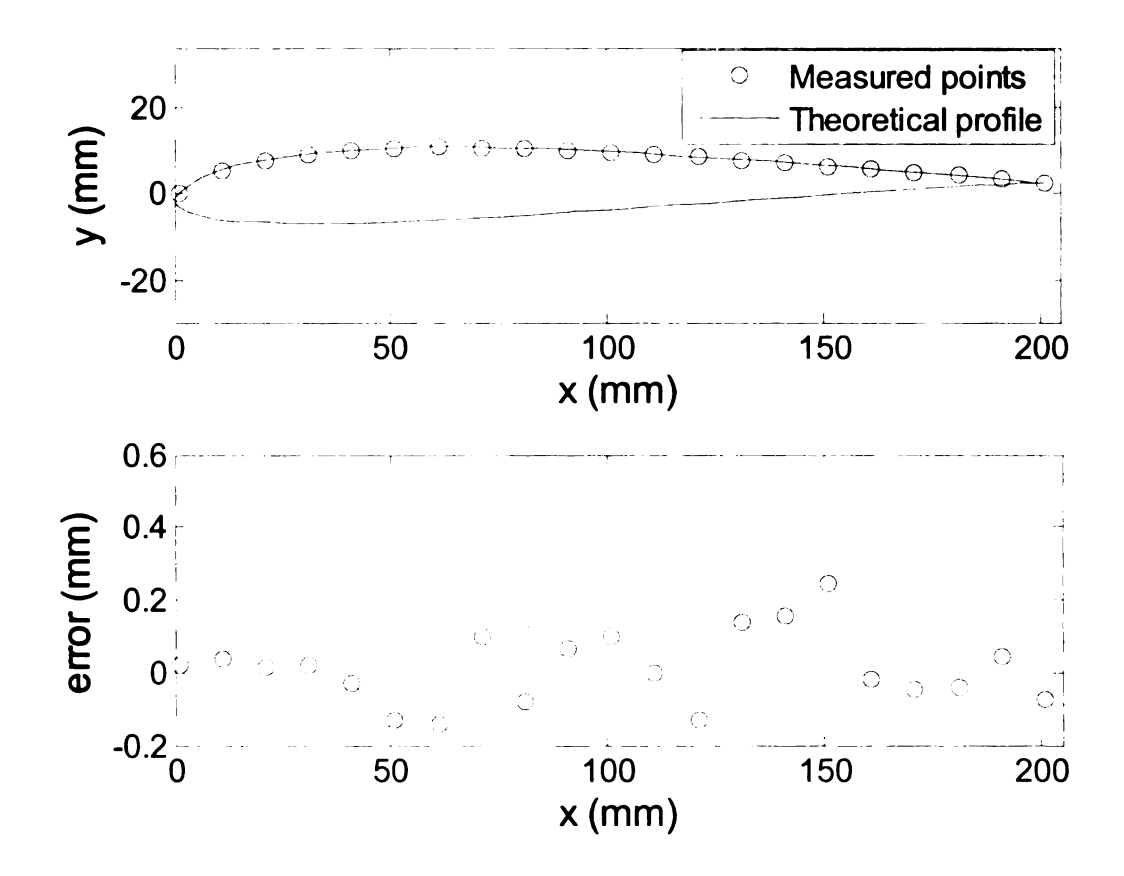


Figure 2.10: Measured suction-side surface points and corresponding difference error

As Figure 2.10 demonstrates, the measured airfoil surface fits well with the theoretical profile. Analysis shows the root mean squared disagreement between the two profiles is <0.1 mm, or <0.05% of the chord length.

After refinishing the surface of the airfoil, a test rig was needed that suspended the airfoil in the flow, allowed the angle of attack to be varied, and also did not obstruct the view of

the flow around the airfoil. With these requirements in mind, a structure was designed and built with Plexiglass walls, an aluminum support structure, and brass lever arms for changing the angle of attack. The airfoil rig allows for an angle range of -45° < α < 45° by varying the brass arm assembly. The airfoil rig is shown in Figure 2.11.

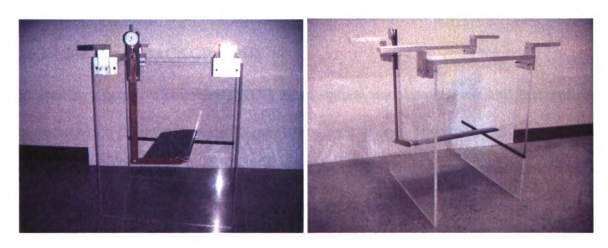


Figure 2.11: Airfoil rig.

The angle of attack was determined in two steps. First, an optical method was used to determine the angle of the airfoil relative to a reference line. The reference line was parallel to the bottom of the tunnel, and was marked on the inside surface of one of the supporting walls in the airfoil rig. An image was then acquired that included both the airfoil and the reference line. By visually estimating the chord line of the airfoil as well as the edge of the reference line, the angle referenced to the bottom of the tunnel can be determined using the image software ImagePro. Each line could only be estimated to within $\pm 0.2^{\circ}$, making the total uncertainty of the angle measurement $\pm 0.4^{\circ}$. Because the flow in the tunnel is not perpendicular to the bottom of the tunnel, the angles determined

by this visual method are not the true angles of attack. For additional information on how the angles of attack (referenced to the freestream direction) were determined, see sections 2.1.1 and 3.1.

2.2. MOLECULAR TAGGING VELOCIMETRY TECHNIQUE

2.2.1. METHOD BACKGROUND

Molecular tagging velocimetry (MTV) is an optical measurement method that utilizes molecules in a fluid that can be "tagged" by a light source. The molecules are usually a chemical tracer dissolved in the fluid. After tagging, the flow is interrogated by a camera at two subsequent times, capturing an image pair composed of one "undelayed" and one "delayed" image. The image pair can then be processed, usually by a correlation technique, to find the displacement of the tagged regions. With a known time delay Δt between the images, the velocity can be determined. Figure 2.12 shows a typical MTV image pair and the resulting vector field. With a grid such as that shown in Figure 2.12, the two-component velocity field is measured. From this information, additional data can be calculated, such as the streamlines and out-of-plane vorticity field.

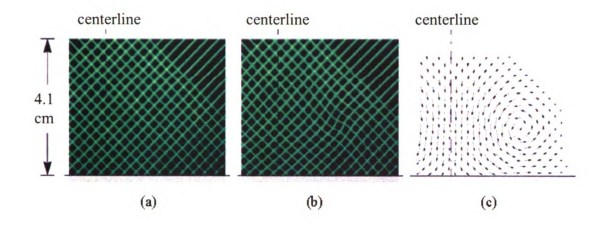


Figure 2.12: A typical MTV image pair is shown, along with the corresponding vector field determined by the pair. (a) The undelayed image is taken 1μs after excitation. (b) The tagged grid is shown after 8 ms. (c) The resultant vector field found from (a) and (b). [Gendrich et al., 1997].

The chemical tracer used in this work is bromonaphthalene, the molecules of which, when excited to a higher energy state by an ultraviolet laser, emit bright green light through the mechanism of phosphorescence. Phosphorescence is an exponentially decaying emission, characterized by a longer timescale (lifetime) of luminescence than fluorescence. Though fluorescence is present for bromonaphthalene, it exists only in the nano-timescale (~10 ns lifetime), while the typical phosphorescence lifetime is nominally 5 ms. This allows delays to be used that are on the order of 10 ms.

The fluid used in this study is water (see section 2.1.1 for details on the water tunnel), in which bromonaphthalene has low solubility. In addition, the dissolved oxygen present in water at standard conditions absorbs the vibrational energy of the excited molecules, returning the molecules to their ground state, preventing any phosphorescent emissions.

To address this so-called oxygen "quenching," a sugar and an alcohol are added to the water with the bromonaphthalene. The sugar, in this case cyclodextrin, has a cup-shaped molecular structure, and dissolves readily in water. The interior of the cup is hydrophobic, and thus the bromonaphthalene is attracted to the inside of the cup. The alcohol, cyclohexanol, bonds to the sugar and acts as a lid for the cup. The cup-and-lid structure shields bromonaphthalene from oxygen quenching, and the long-lifetime green phosphorescence is observed. The structure formed by these three chemicals is referred to as a phosphorescent supramolecule [Gendrich *et al.*, 1997]. This supramolecule is employed in this study as a tracer.

2.2.2. ONE-COMPONENT MTV MEASUREMENT TECHNIQUE

As discussed in Chapter 1, the goal of this study is to gain high-resolution near wall data about the flow of interest. To achieve this, a one-component MTV approach was used. The one-component MTV measurements in these experiments involve tagging and interrogating lines in the flow that are nominally normal to the freestream direction. This allows for the streamwise velocity component to be extracted from each row of pixels in the images, which, combined with a small field of view, can yield a high spatial resolution. This differs from two-component and stereo (three-component) MTV techniques, in that only the component normal to the tagged lines is measured. This requires making the assumption that the flow is mostly uni-directional, as well as awareness that, in regions where other velocity components are large, this technique will be more inaccurate. The error due to the component of the velocity parallel to the lines can be expressed in Equation (5) [Hill et al., 1996], with error Δu , instantaneously

measured velocity u, parallel velocity component v, and delay between the images Δt .

Figure 2.13 shows a sample of typical one-component MTV image pairs.

$$\frac{\Delta u}{u} = \frac{v}{u} \frac{\partial u}{\partial v} \Delta t \tag{5}$$

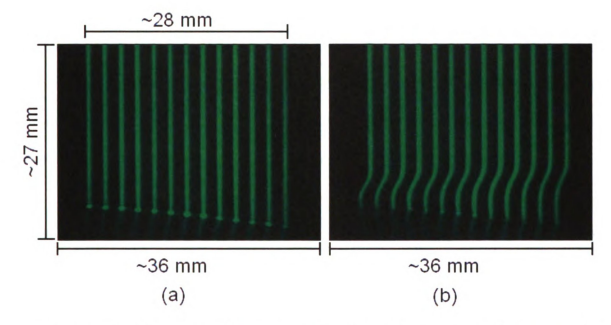


Figure 2.13: Example of a one-component MTV image pair. $\alpha = 6^{\circ}$, Re=20,000, $x \approx c/3$. (a) The undelayed image is shown 2 μ s after the laser pulse. (b) The delayed image, taken 10 ms later, shows the instantaneous streamwise velocity profile.

Note that in Figure 2.13 the field of view is less than 3 x 4 cm. Each pixel in these exemplary images represent \sim 50 μ m, meaning that in the wall normal direction the spatial resolution is as fine as 0.00025 normalized by chord length of the airfoil.

2.2.3. IMAGE ACQUISION

Due to the small field of view being captured, the images being acquired have a low amount of light. This is especially true for the delayed images, since they are taken at or beyond the phosphorescent lifetime of the chemical tracer. In this work, a Stanford Computer Optics 4QuikE intensified CCD (charge coupled device) camera was employed. This camera uses an image intensifier to amplify the light sent to the CCD chip. Photons entering the intensifier are converted to photo electrons by the photocathode. These photo electrons are then multiplied by the micro channel plate, and then finally converted back to photons by the phosphor screen. By varying the voltage to the intensifier, the amount of amplification can be increased or decreased. As with all amplification devices, the image noise is increased with higher amplification.

In addition to light amplification, the intensifier also provides a useful shuttering function. The intensifier can be triggered by an external signal while the CCD chip runs continuously at 60 Hz frame rate. Because the CCD chip only receives the light sent to it by the intensifier, the effective exposure time for the image is controlled by the intensifier. In the case of intensified cameras, this exposure time is referred to as the gate period. The external signals are generated in reference to the 60 Hz internal clock of the CCD chip, which is called the Fsync signal. By placing a gate period at the end of one frame (undelayed) and near the beginning of the next (delayed), image pairs can be acquired with a small delay. This is known as running the camera in "double shot" or "quick shot" mode. In this case, the undelayed image is triggered 2 µs after the laser pulse to avoid capturing the bright blue fluorescence that occurs during excitation. When

the camera is acquiring images at a 60 Hz frame rate in double shot mode, the velocity data sampling rate is 30 Hz, since each sample is made up by an image pair. A schematic of the camera and laser timing is shown in Figure 2.14.

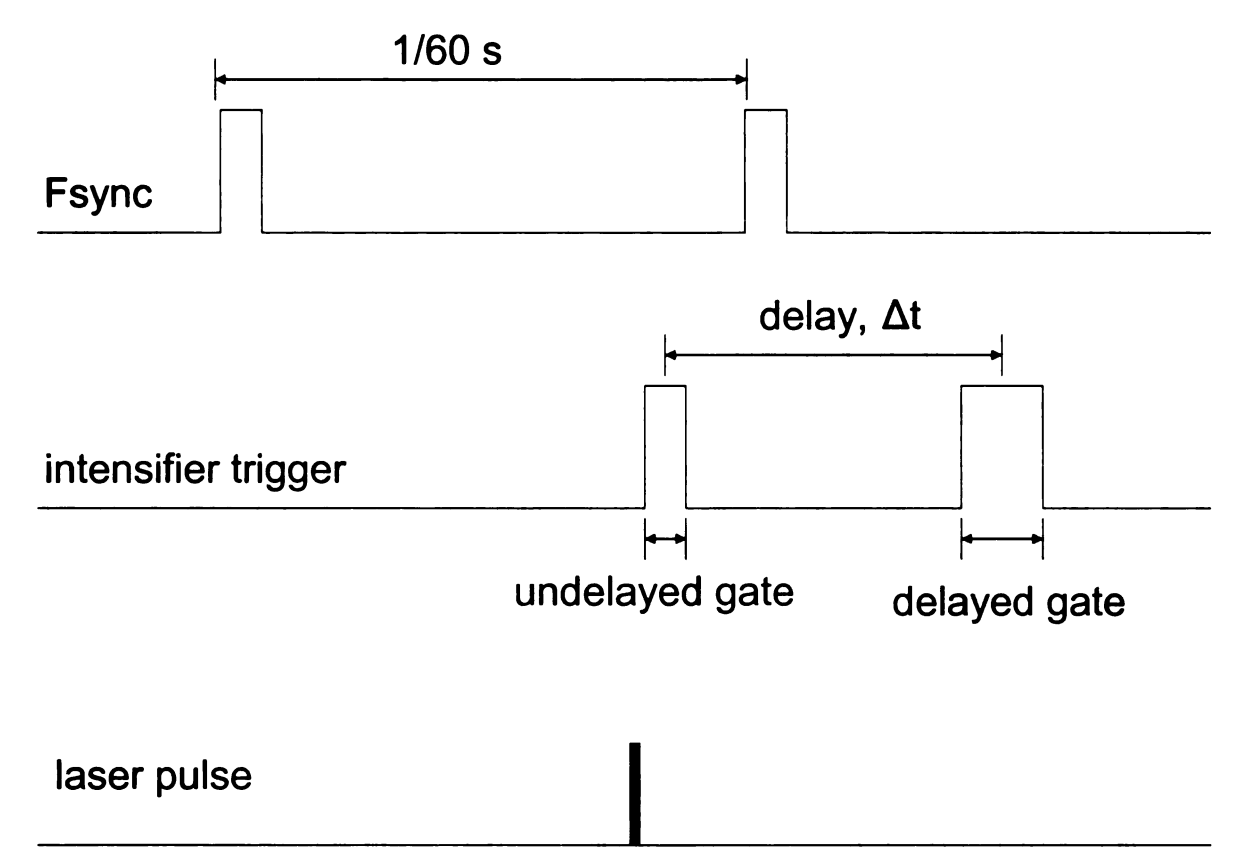


Figure 2.14: Camera timing diagram. The Fsync signal is the internal clock of the CCD chip, which is used as a reference to create the other timing signals. The undelayed image is taken 2 μ s after the laser pulse to avoid fluorescence emission. The delay is defined as the center-to-center distance between the undelayed and delayed gate periods. The widths of the Fsync pulses are \sim 0.8 ms; this corresponds to the time needed to send the image data from the camera to the acquisition system.

When choosing a delay, it is important that is it long enough to allow the tagged region to displace, while also being short enough so that the tagged lines will not run into each other in regions of high displacement. It is also important that the delays are short so the average calculation of velocity ($v = \Delta x/\Delta t$) is still accurate. This can be a very difficult

task, especially in a flow such as this one, in which there exists areas of steep velocity gradients. For these experiments, the delays were chosen so that the displacement in the freestream would be nominally half of the line spacing, or 0.005c. This gives large enough displacements for accuracy without the risk of running into other lines during correlations. The delays used at different Reynolds numbers, as well as the gate periods (exposure times) used are given in Table 2.2.

Table 2.2: Delays used between the MTV image pair at different Reynolds numbers. The delays were decreased as the freestream speed of the tunnel was increased to keep the displacement nominally at half the line spacing. Also given in the table is the gate (exposure) period for the undelayed and delayed images.

| Re | 20,000 | 30,000 | 40,000 | • |
|----------------|--------|--------|--------|----|
| delay | 10.15 | 7 | 5 | ms |
| undelayed gate | 0.1 | 0.1 | 0.1 | ms |
| delayed gate | 0.8 | 0.5 | 0.3 | ms |

Because the sampling frequency f_s is fixed at 30 Hz and the record length has been previously determined to be 150 seconds (see section 2.1.1), the total number of image pairs is 4500 per field of view. Because of the large size of the image files for a single field of view (~2.5 GB), the images were acquired by a MuTech board installed on a PC, and written directly to disk.

As previously discussed, small fields of view are used in this study to extract data at very fine spatial resolution. Therefore, to capture information all along the surface of the airfoil, the laser optics and camera system was traversed with the help of a linear traverse set-up attached to the test section. This traverse system utilizes two lead-screws to be able

to move left-right and up-down with precision. Although the traverse is incremented to 25 microns, a more accurate estimation of the precision was found to be ± 350 microns, or ± 6 pixels. This was determined by repeating the same types of motions utilized in the actual experiment and determining the fluctuations in the distance moved. Both the camera and the optical arrangement discussed in section 2.1.1 were attached to this traverse, and therefore never moved with respect to each other.

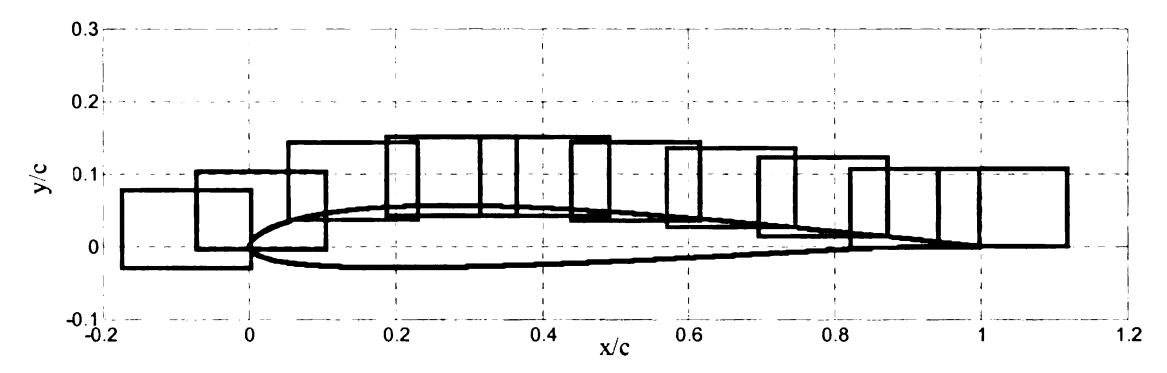


Figure 2.15: Ten overlapping fields of view (alternating blue and red) required to capture all the velocity at the surface of the airfoil.

Ten overlapping fields of view were required, as shown in Figure 2.15, to capture all the data near the surface of the airfoil, and additional fields of view were included above those shown as needed. The uncertainty in the movements introduced by the traverse system used was corrected after the velocity data were available. The fields of view were shifted so that the velocity profiles matched well and transitioned smoothly from one field of view to the next. The shifts did not exceed the uncertainty in the traverse system.

As discussed in section 2.2.2, the MTV mechanism used in this work relies on excitation by ultraviolet light. A Lambda-Physik model LPX-200 excimer laser was used. This laser emits 20 ns pulses of 308 nm ultraviolet light at up to a 100 Hz repetition rate. For these experiments, a repetition rate of only 30 Hz was necessary, as this was the maximum data acquisition rate attainable by the camera. The maximum energy per pulse is 300 mJ, but for this study 200 mJ was sufficient to attain a good signal to noise ratio.

2.2.4. ONE-COMPONENT PROCESSING

In order to process the image pairs, a processing code was written in MatLab. Due to the nature of the one-component method, it was a challenge to create a code that was both robust and fast. The method used was a row-by-row, line-by-line cross-correlation approach. For a given line, the first row intensity profile on the undelayed image was extracted, as was the corresponding profile (same tagged line, same pixel row) on the delayed image. Everything except that single profile was masked out with a "floor level" or background level. This results in two profiles such as those found in Figure 2.16, which are taken from the images found in Figure 2.13.

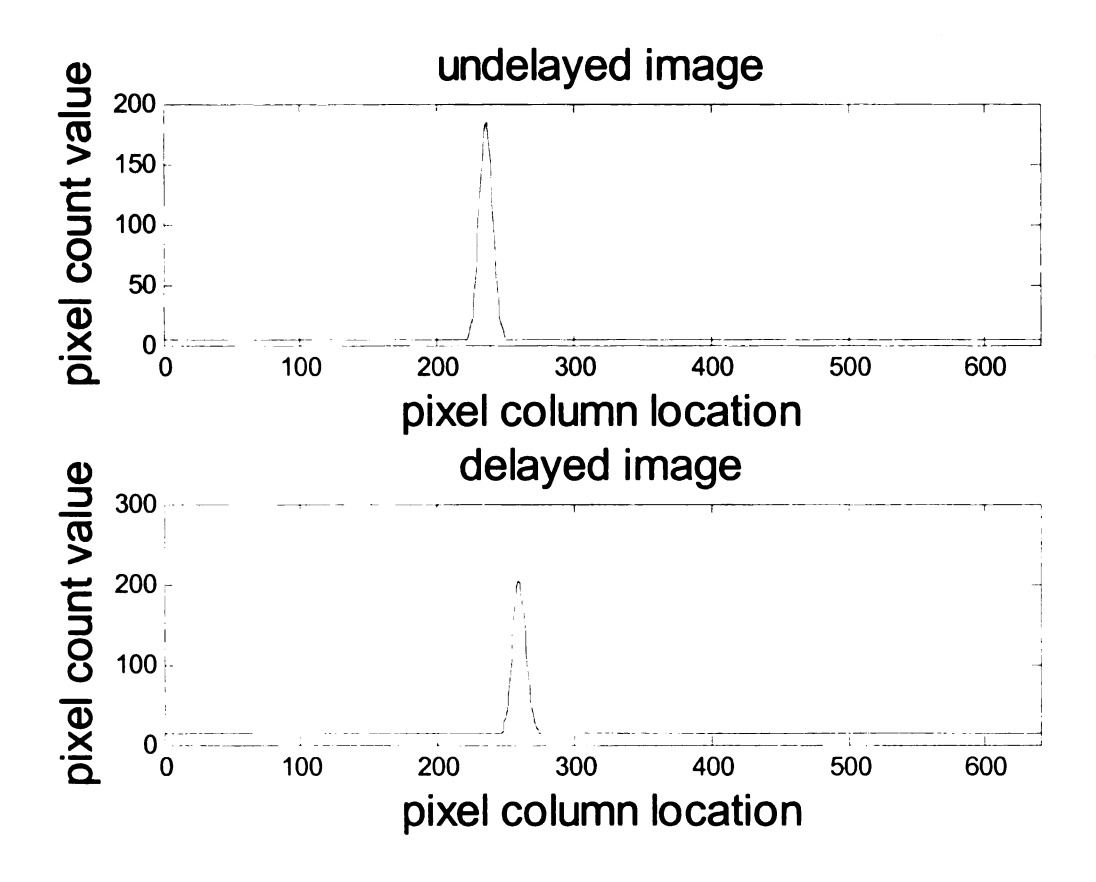


Figure 2.16: Undelayed and delayed intensity profiles, taken from the middle of the fifth line from the left in the images in Figure 2.13. All the other lines' intensities are masked out and replaced by a constant background value.

After the two profiles have been extracted, the mean is removed from each signal and their correlation function is determined using the Fourier transform. The correlation is shown in Figure 2.17(a). To achieve sub-pixel accuracy, a least-squares fit of a 7th order polynomial is found for the peak of the correlation. A more detailed view of this is shown in Figure 2.17(b). This process is then repeated for every row of every line for a given image pair. Each image pair typically has 13 lines, with ~400 rows each, resulting in ~5000 vectors calculated per image pair. Each image pair takes ~35 seconds to complete processing. With this in mind, it is easy to see how processing time becomes an issue.

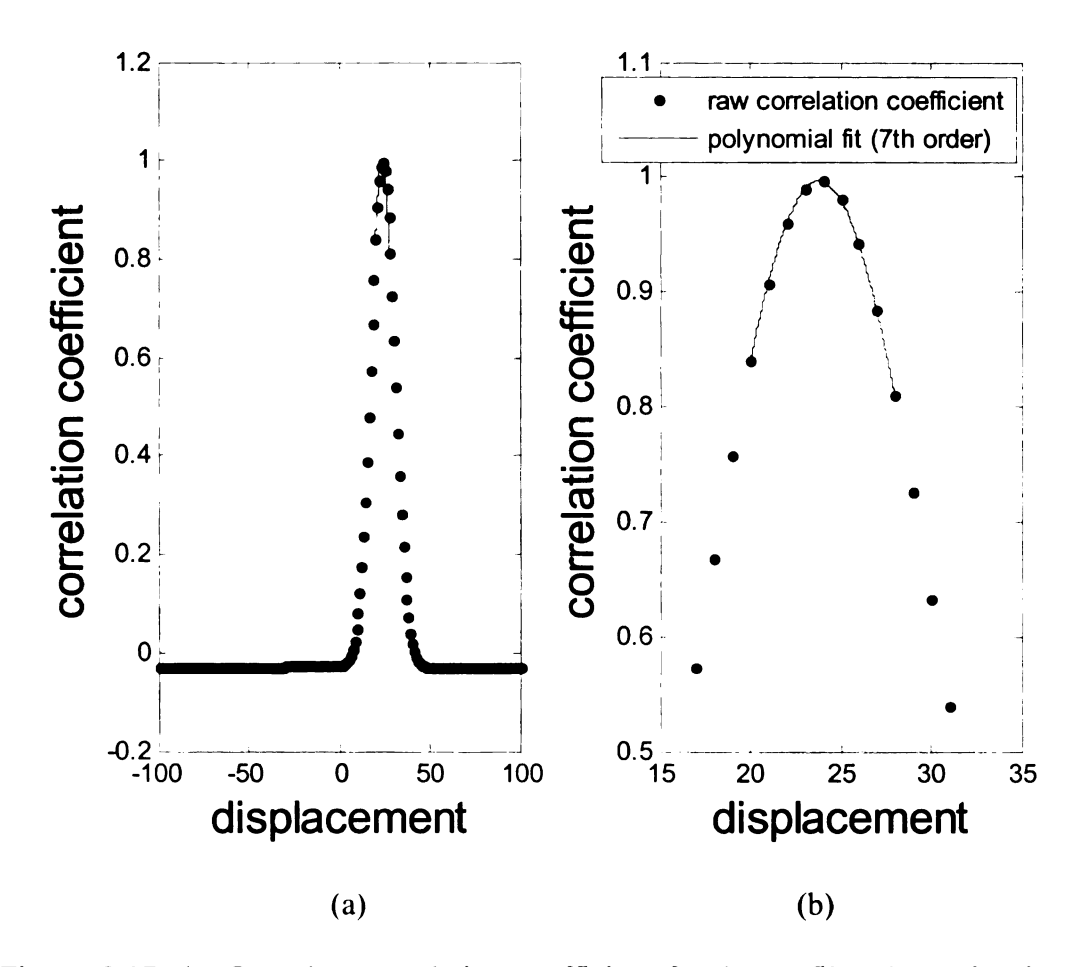


Figure 2.17: (a) Complete correlation coefficient for the profiles shown in Figure 2.16. (b) Detailed view of the 7th order polynomial fit to the peak for subpixel accuracy.

Because of this lengthy processing, it was desired to process the data at a lower rate than it was acquired, effectively reducing the sampling rate f_s of the measurements. Caution also had to be exercised to make sure the statistics of the data were preserved after decimation. Time series data from a field of view which included both the separated shear layer and the freestream were used to determine the effect of down sampling. The time series, one from the freestream region and one in the shear layer, were decimated using several lower sampling frequencies and the statistics in each case were compared.

The results from this analysis are shown in Table 2.3. For each down sampled rate, the percent difference of a statistic from the same statistic at the original sampling rate is given. In the shear layer, the difference in the statistics never reaches more than ~1%. In the freestream, the difference is less than 0.1% for the mean, and never greater than 2.9% for the RMS. The reason a larger difference is seen in the RMS than the rest of the flow statistics is the magnitude of the RMS is very small for the freestream.

Table 2.3: The effect of down sampling on the mean and RMS velocity in (a) the shear layer and (b) the freestream. The mean and RMS are presented with their percent difference from the original rate of 30 Hz.

| f _s (Hz) | 30 | 15 | 10 | 7.5 | 6 | 5 |
|---------------------|-------|-------|-------|-------|-------|-------|
| RMS (mm/s) | 27.18 | 27.26 | 27.04 | 27.39 | 27.47 | 27.14 |
| % difference | - | 0.30 | 0.52 | 0.77 | 1.08 | 0.13 |
| mean (mm/s) | 90.68 | 90.61 | 90.58 | 90.55 | 90.77 | 90.58 |
| % difference | - | 0.08 | 0.12 | 0.15 | 0.10 | 0.12 |

(a)

| f _s (Hz) | 30 | 15 | 10 | 7.5 | 6 | 5 |
|---------------------|--------|--------|--------|--------|--------|--------|
| RMS (mm/s) | 3.95 | 4.02 | 3.98 | 4.07 | 4.00 | 4.05 |
| % difference | - | 1.60 | 0.52 | 2.90 | 1.26 | 2.42 |
| Mean (mm/s) | 142.42 | 142.43 | 142.44 | 142.31 | 142.29 | 142.43 |
| % difference | - | 0.0050 | 0.0076 | 0.0775 | 0.0922 | 0.0007 |

(b)

Due to the significant time benefit of processing at a decimated rate while still maintaining the statistics of the flow, 5 Hz was chosen as the rate at which the data should be processed. Thus, at the chosen sampling time of 150 s, image pairs are acquired at 30 Hz for a total of 4500 image pairs per field of view. The samples are then decimated in processing to 5 Hz for a total of 750 image pairs processed per field of view.

Currently, the one-component MTV software takes ~six hours to complete processing data from a given field of view with 750 samples (image pairs). The work in this study is made up of 148 such fields of view, resulting in over 900 hours of data processing, just to obtain the raw displacement data.

3. DATA AND RESULTS

After acquiring the data and processing the image pairs using the program and methods described in section 2.2.4, the data were ready for analysis. To start, the mean and RMS of the streamwise velocity were determined, and the different fields of view for each case were assembled using knowledge of the precise movements made with the linear traverse mount. The assembled mean and RMS contour and "vector" plots gave an overview of the characteristics of the flow, and were also used for determining the separation and reattachment points.

3.1. POST-PROCESSING AND ANGLE ISSUES

After the initial processing of the image pairs (see section 2.2.4), some additional post-processing was necessary. Due to the uniqueness of the flow for each Reynolds number and angle of attack combination, a different post-processing program was needed for each case. During initial processing of the data, the correlation processing was performed over a domain larger than the flow extent in the cross-stream direction (i.e., into the airfoil wall) so that no data near the surface were excluded. Thus, removing the non-physical data was one of the most important parts of post-processing. Near the surface, bright spots caused by the laser were a hindrance to determining the exact wall location. An average image in Figure 3.1 shows the bright spots near the surface.

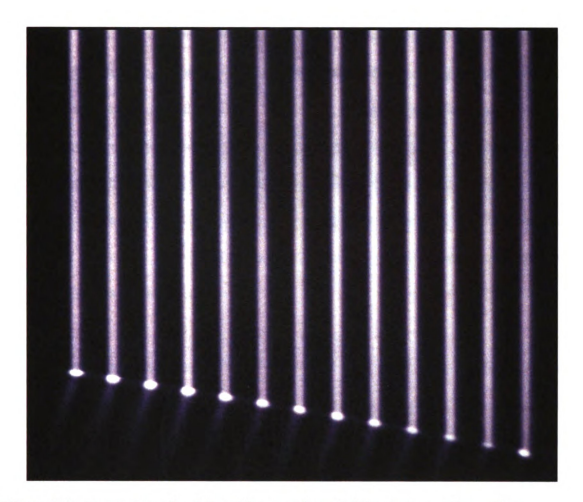


Figure 3.1: An average of undelayed images shows bright spots near the surface.

The bright spots ranged in size from about 5-10 pixels (0.3-0.6 mm). The centers of the bright spots were taken as the wall locations, the velocities at these points were set to zero, and the data below were truncated. In addition to removing meaningless data, this also allows the estimate of an experimental airfoil profile. The experimental profile (not to be confused with the measured profile, as described in section 2.1.2) is formed by the positions of the last (lowest) data points above the surface after wall truncation.

In order to find and present the separation and reattachment points in a manner consistent with most literature on the topic, the coordinate system shown in Figure 2.8 needed to be rotated and translated such that the leading edge is the origin, and the x-axis is along the mean chord line. The rotated coordinate system is denoted by unprimed symbols. Because the trailing edge location is easier to determine due to being a sharp edge, it was selected as a reference point instead of the leading edge. During the experiments, one of the tagged lines was positioned at the trailing edge, and all other movements were referenced to this initial position.

Since the trailing edge is known to within a line width and the chord length is known, with the angle of attack of the airfoil, the leading edge could also be determined. Instead of assuming the angle was that which was determined during calibration (see section 2.1.2), a least-squares fit of the theoretical profile to the experimental profile was used in each case. This was done for several reasons: It allows for validation of the initial angle calibration, it can be used to validate that the experimental surface deviation does not greatly exceed the deviation of the measured profile from the theoretical profile, and the appropriately positioned and rotated airfoil can be plotted in figures for reference and display purposes. To find the least-squares fit, the angle of attack was varied over $\pm 2^{\circ}$ and the trailing edge position was changed within ± 0.3 mm (one laser line thickness). For each pair of values of the angle of attack and trailing edge position, the theoretical profile coordinates were computed. The mean squared deviation between the theoretical profile and the experimentally determined profile were calculated. The actual angle attack and trailing edge locations were then determined as those resulting in the least mean squared

deviation. The results showed that the angles being determined by this method were yielding angle results that were on average 0.46° less than the calibration angle. These disagreements are shown in Table 3.1, which presents the angles determined by the initial calibration, and the angles determined after the experiment by the use of a least-squares fit to the experimental profile. The RMS error of the each fit is also shown to illustrate that the experimental profile's error does not greatly exceed the error found in the measuring the airfoil profile on the milling machine (<0.1 mm, see section 2.1.2). Slightly higher disagreement in the fit to the experimentally determined profile is expected, since in addition to the physical profile differences, there is also uncertainty in determining the experimental surface points.

Table 3.1: Discrepancies between the calibrated angles and those determined by a least-squares fit to the experimental profile. calibrated angles are those determined by the initial imaging-based calibration. The experimental data are the angles determined by the fit and the RMS error of the fit.

| Re (× 10 ⁻³) | | 30 | | | |
|--------------------------|------|------|------|-------|------|
| calibration α (°) | 4.05 | 6.05 | 7.95 | 11.05 | 3.94 |
| experimental α (°) | 3.75 | 5.65 | 7.3 | 10.55 | 3.49 |
| RMS error (fit) (mm) | 0.11 | 0.12 | 0.13 | 0.16 | 0.09 |

| Re (× 10 ⁻³) | 30 | 40 | | | |
|--------------------------|------|------|------|------|-------|
| calibration α (°) | 7.84 | 3.94 | 5.94 | 7.84 | 10.94 |
| experimental α (°) | 7.39 | 3.59 | 5.49 | 7.29 | 10.44 |
| RMS error (fit) (mm) | 0.13 | 0.12 | 0.12 | 0.13 | 0.11 |

mean α difference: 0.46 RMS of α difference: 0.10

To determine if the discrepancy in α was caused by the method of curve fitting to the experimental profile, several simulations were performed. The program used created a simulated version of the experimental profile with a comparable number of points (85) by adding Gaussian noise of different mean and RMS values to the theoretical profile. This is to replicate the uncertainty in choosing the surface points. This program then used the least-squares method of fitting the theoretical profile to the simulated experimental profile. A sample simulated experimental profile and its matched theoretical profile are shown in Figure 3.2. Note that the axes of this figure are scaled differently to display the noise in the profile. As can be determined from this figure, the simulations were performed in pixel units, as this is the method used in the actual post-processing code.

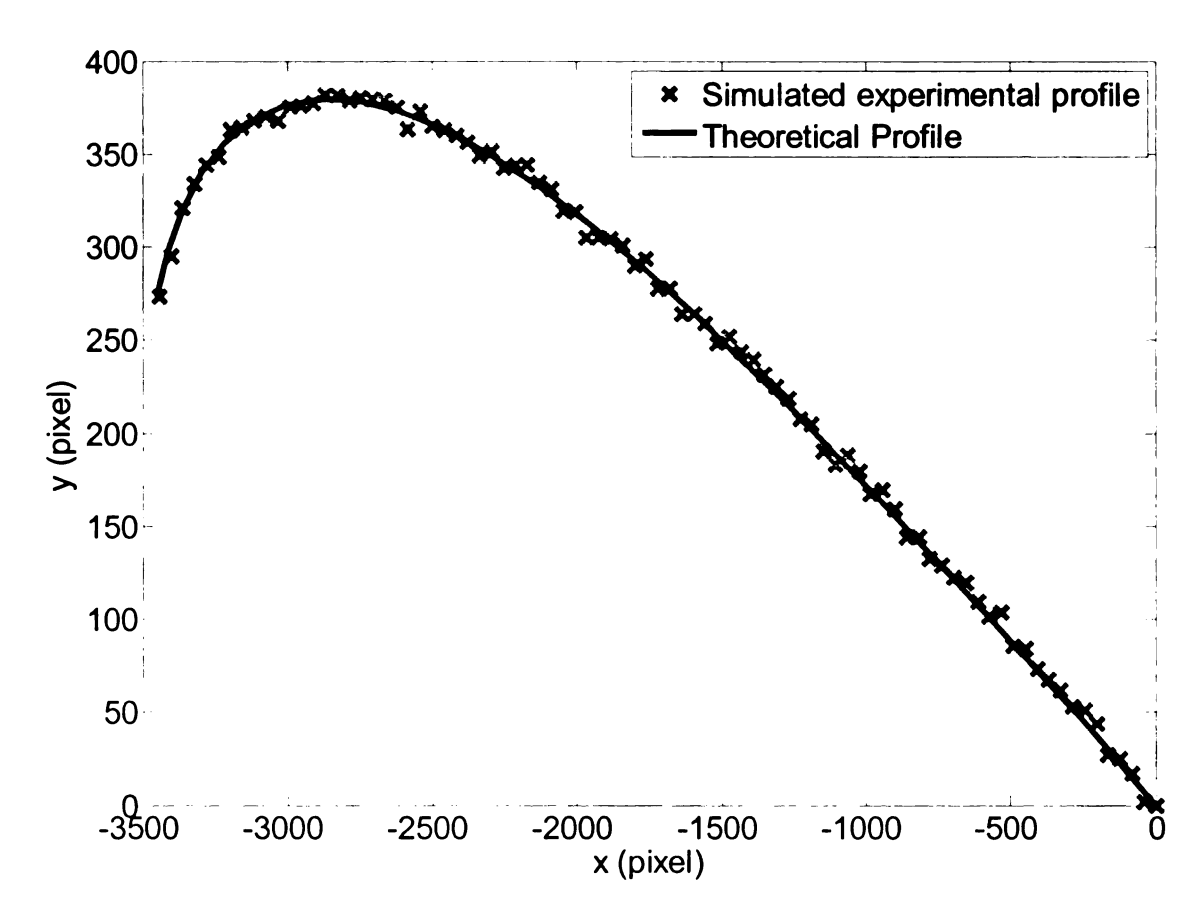


Figure 3.2: Matched theoretical profile with simulated experimental profile for RMS_{noise} = 4 pixels, mean_{noise} = 10 pixels

Because the actual chord length of the airfoil used in the experiments is known, it is set as a fixed value, as the position of the trailing edge (within one line thickness) and the angle of attack are varied to find the best fit. To investigate the effect of having estimated the airfoils length poorly, three fixed chord lengths were tested in the simulation. That is, if the value used is off by \pm 0.5 mm (\sim 8 pixels), how this error will affect the fit. In this simulation, the mean of the noise was fixed to be zero. The results from this simulation are shown in

Table 3.2.

Table 3.2: Simulation testing the robustness of the fitting routine used in the experiment. The mean of the noise was zero in all cases. The angle is recovered well within the accuracy of the fit, with the shorter and longer chord lines resulting in changes mostly in the horizontal offset used.

| angle specified (°) | chord length specified (pixels) | RMS of noise (pixels) | fixed chord line specified for fit (pixels) | angle determined (°) | offset used (pixels) | mean of noise (pixels) |
|---------------------------|--|-----------------------|---|----------------------------|----------------------------|---------------------------------|
| 3.82 | 3477.3 | 2 | 3469 | 3.80 | -5 | 1.9367 |
| 3.82 | 3477.3 | 3 | 3469 | 3.85 | -3 | 2.768 |
| 3.82 | 3477.3 | 2 | 3477 | 3.80 | 0 | 2.0464 |
| 3.82 | 3477.3 | 3 | 3477 | 3.85 | 0 | 3.1916 |
| 3.82 | 3477.3 | 2 | 3485 | 3.80 | 2 | 2.2806 |
| 3.82 | 3477.3 | 3 | 3485 | 3.80 | 5 | 3.5606 |
| | | | mean | 3.82 | -0.17 | 2.63 |
| | | | RMS | 0.03 | 3.54 | 0.65 |

These results show that when forcing the chord length to a fixed value within 1 mm of the actual value and using the angle of attack and horizontal position of the trailing edge as fit parameters, the angle is recovered, with a maximum deviation of 0.03°.

Additional simulations that varied the vertical position of the trailing edge, the chord length of the airfoil, and included more extensive variations in the noise level of the simulated profile, yielded similar results, with overall RMS deviation of 0.07° from the actual value in the angle being determined. By performing these simulations, it was shown that the method of fitting the experimental profile to the theoretical profile was a robust means of recovering the angle of attack, and the discrepancy found in the angle of attack in the experiments was not caused by the fit method.

One additional option to explore was the possibility that the initial calibrations, as described in section 2.1.2, suffered from some inaccuracies. Because the angles were determined using an optical method of estimating the chord and reference line, there could have been a large uncertainty. To determine if this uncertainty was the root of the disagreement between the imaging-based angles and those found from the least-squares fit, a program was written to find the angle of attack more precisely from the calibration images.

Before finding the angle, some processing was performed on each calibration image. The image was filtered with an edge detection routine, and then segmented into binary form, i.e., "edge" = 1, and "not an edge" = 0. A processed calibration image is shown for the 8 degree angle of attack case in Figure 3.3 (the image is inverted for display purposes). The top edge of the airfoil and the reference line was then more easily extracted in the processing program. After extracting the surface, the least-squares fit method was used to determine the angle of the airfoil. This fit also allowed the chord line to vary, and in similar fashion to the second simulation mentioned above, a floating trailing edge was used in the fit since the edge detection filter did not pick up the sharp edge, as shown in Figure 3.3. A simple linear fit was performed for the reference line. The angle between the airfoil's chord line and the reference line could easily be determined with trigonometry.

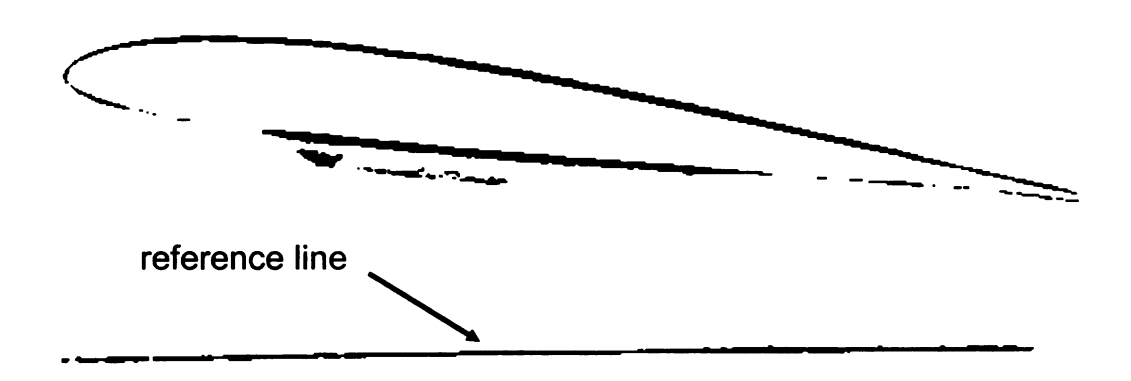


Figure 3.3: Processed calibration image for use in determining the angle of attack for the 8 degree case (inverted contrast). The edge detection was unable to pick up the trailing edge.

This was performed for all four calibrations of nominally 4, 6, 8, and 11°, and the results are shown in. Note that these are angles between the chord line of the airfoil and the reference line in the image without accounting for the freestream flow angle. Therefore these values are not the same as those shown in Table 3.1. The green highlighted data are that of the initial calibration, and the non-highlighted data are the results of the higher precision program. The angle of the reference line, chord line angle, and chord length determined by this program is also included to demonstrate consistency across the four calibrations. From examining the data in this table, it is clear that the calibration angles were not the cause of overestimating the angle of attack by ~0.5°. If anything, these results show that the calibration images were underestimated.

Table 3.3: Initial calibration angles and corresponding fit-determined angles using the same images. These angles are relative to the reference line and therefore not the angle of attack. The reference line angle, chord line angle, and chord length are also shown to demonstrate consistency across the four calibrations.

| angle (calibration) (°) | 3.80± 0.4 | 5.80 ± 0.4 | 7.7 ± 0.4 | 10.8 ± 0.4 |
|-------------------------|-----------|----------------|---------------|------------|
| angle (fit) (°) | 4.22 | 6.02 | 8.05 | 11.07 |
| ref. line angle (°) | 0.77 | 0.72 | 0.75 | 0.72 |
| chord angle (°) | 3.45 | 5.3 | 7.3 | 10.35 |
| chord length (pixels) | 525 | 525 | 525 | 514 |

Because the investigation into this issue did not yield results that explained the overestimation of the angles of attack, a possible reason is given here. If the reference line itself was misaligned to the bottom of the tunnel, this would cause a bias error in the calibration. It is posited that this was the case at the time of calibration. Because the method of determining the angle by the least-squares fit to the theoretical profile was proven to be robust, the angles found by this method, with the freestream angle factored in, are quoted as the actual angles of attack in this work. These angles are known to within $\pm 0.14^{\circ}$ (95% confidence level).

In addition to the calibrated angles shown in

Table 3.3, an early experiment was performed for an estimated angle of attack of 8° was performed. The purpose of this experiment was to orient the experimentalist to the types of issues that would come up in the data taking, processing, and analysis processes. Because of this, little attention was paid to the angle initially, and using the least-squares

fit method, the angle was determined to be 8.80° retroactively. This data point is included in future plots and tables for completeness.

3.2. SEPARATION AND REATTACHMENT

To determine the separation and reattachment points, the mean velocity "vector" plots were used. Starting from the airfoil's leading edge and progressing downstream, the point of separation is found at the location where the first reliable near-surface velocity becomes reversed. Progressing downstream from the separation point, the position of reattachment coincides with the location where the first reliable near-surface velocity profile is in the streamwise direction. Reliability refers to the effect that the bright spots (discussed in section 3.1) have on the accuracy of the correlation technique near the wall. Near the airfoil surface, the bright spots cause unreliable vectors at the 3-12 lowest data points, which are visually distinguishable from the reliable vectors. Near the surface, the velocity should approach zero because of the no-slip condition. However, the unreliable vectors typically do not approach zero. Figure 3.4 shows an example of this occurring. The mean velocity vectors are plotted for a given profile, and overlaid on the corresponding averaged undelayed image for reference. As the position of the data approaches the wall, the mean vectors smoothly approach zero at first, and then near the bright spot they seem to asymptote to a non-zero value. It is at this height and below where this change of behavior occurs that the data are ignored when determining the separation or reattachment points.

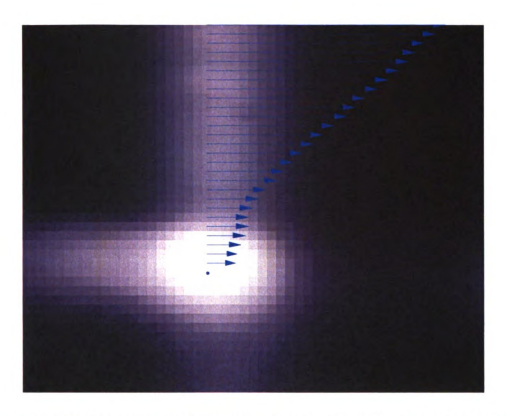


Figure 3.4: Unreliable mean velocity vectors near the surface increase, instead of continuing to smoothly approach zero at the wall. From Re = 20,000 and $\alpha = 3.75^{\circ}$ case.

When plotting near-wall data, the bad vectors are discarded and replaced using an M/10/N-point quadratic curve fit. The M/10/N-point fit is defined here as identifying M near-wall points as bad data, using the 10 points above the bad data (plus the zero velocity point at the surface) for the fit, and "linking" the real data to the fit using N points to make the transition from the real data to the fit look smooth. That is, even though a vector may be reliable, it might need to be overwritten with the curve fit data to make the profile continuous. Because each velocity profile is unique, the numbers of points skipped near the wall as well as the linking points are determined on a case-by-case basis. For this reason, the curve fitting was a time consuming portion of the post

processing. The quadratic model used for fitting omits the constant term to force the velocity to zero at the wall. An example of this curve fitting is shown in Figure 3.5.

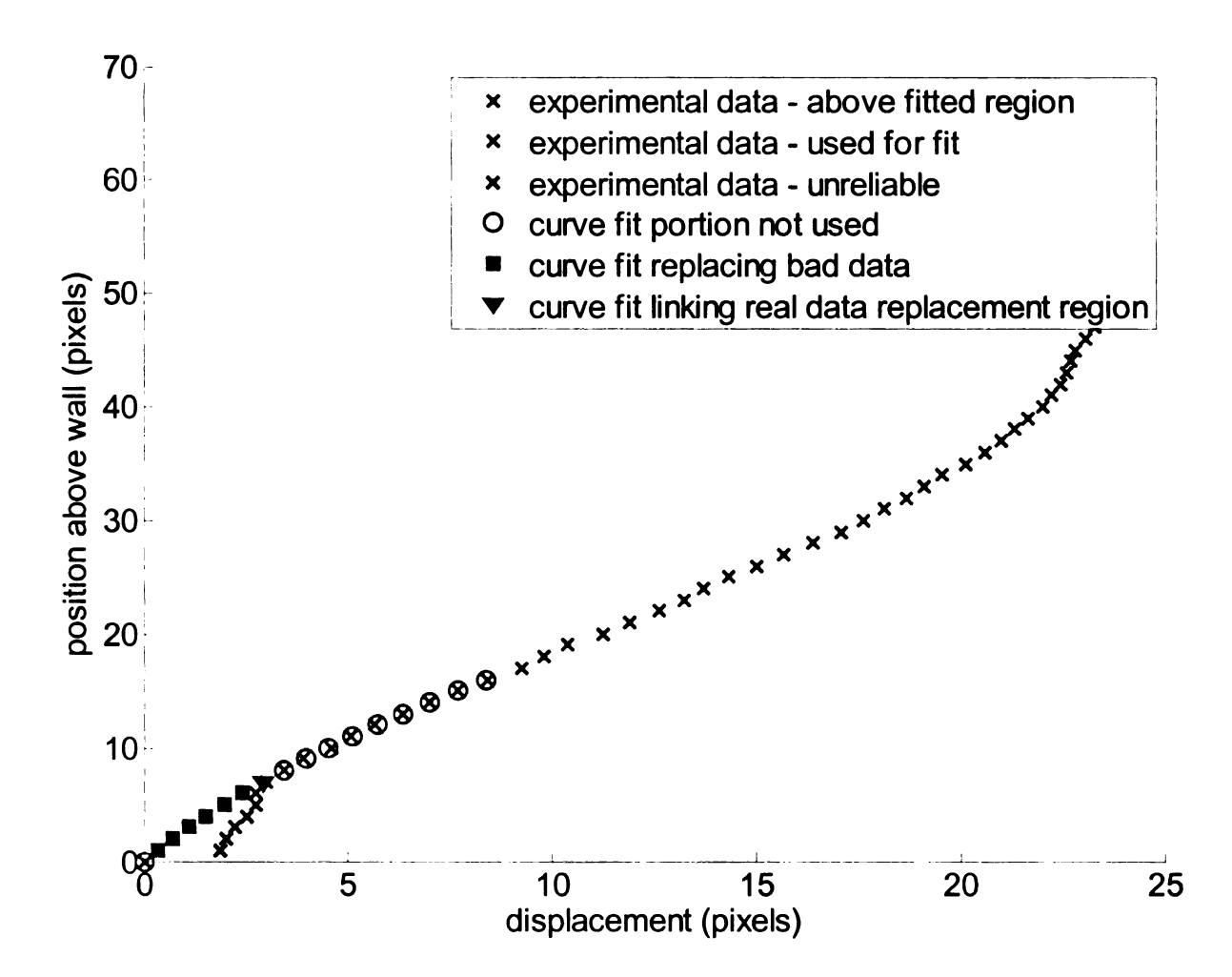


Figure 3.5: Example of bad vector replacement routine. The fit is applied before scaling the raw pixel displacement data. The green experimental data are shown to demonstrate the shape of the profile. The blue experimental data are used for the fit. The black data are bad vectors that have been skipped and replaced. All red data (10 points) are from the curve fit, with the triangular point as a "link" between the bad data and the good data to make the profile smooth.

After applying the curve fit to the data in Figure 3.4, the data continue to smoothly approach zero as the wall is approached, as shown in Figure 3.6. All plots of the mean velocity vectors hereafter will include the curve fit data near the wall. It is also important to note again that the separation and reattachment locations are determined from the data before the curve fit is applied, so that curve fitting does not affect these results.

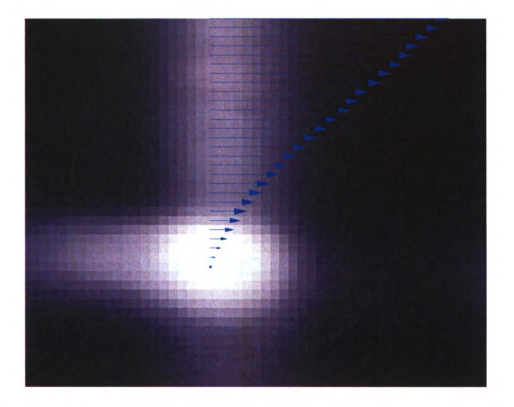


Figure 3.6: Velocity profile from Figure 3.4 after curve fitting is applied. The last seven vectors nearest to the surface were determined to be unreliable, and an additional vector above that was used as a "link" between the real and curve fit data to make the profile smooth, for a total of eight vectors being replaced by curve fit data.

As previously mentioned, to determine separation, the first reversed mean velocity profile is located along the surface of the airfoil. The separation point is chosen to be between this reversed profile and the one immediately upstream of this, which is still attached. An

example of this is shown in Figure 3.7, in which mean velocity vectors are overlaid onto a mean velocity contour map. Similarly, when looking for the reattachment point, the first profile which again returns to the streamwise direction near the surface is sought. An example of how the reattachment point is determined is shown in Figure 3.8. Again the mean velocity vectors are overlaid onto the mean velocity contour map, this time skipping every other vector in the cross-flow direction. Because the velocity values near the wall of the last reversed profile are so small in magnitude, one more upstream profile is included to help see the transition from reversed flow to attached flow. After analyzing

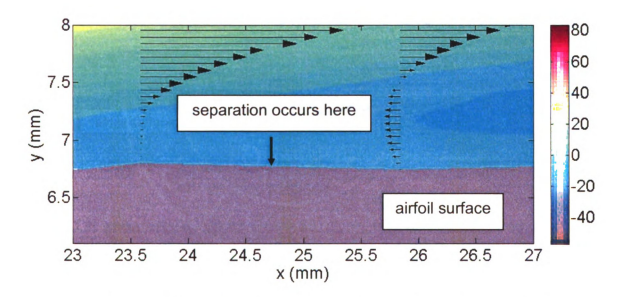


Figure 3.7: Mean velocity profiles, between which separation occurs, overlaid on a mean velocity contour map. The units of the velocity contour "color scale" (displayed on the right) are mm/s. Re = 20,000 and $\alpha = 7.3^{\circ}$ case.

all the cases, the data were compiled and are presented in Table 3.4. Because the velocity profiles are extracted at the laser line locations, the uncertainty in determining the separation and reattachment points is the line spacing, or $\pm 0.0055 \text{ x/c}$ ($\pm 0.3 \text{ mm}$).

It is also important to note that the uncertainty could also be considered two line spacings due to the unreliable vectors near the surface. Because of these vectors, the actual streamwise velocity is unknown very near the wall. Some profiles that asymptote very close to zero before they become unreliable, such as those found just upstream of where separation (or reattachment) has been previously said to occur, may already be reversed (or in the case of reattachment, separated) near the surface. If this near-wall data could be resolved, it is possible that the separation or reattachment location would shift upstream by one line spacing. This possible scenario would give add one line spacing unit to the uncertainty, but biased towards upstream.

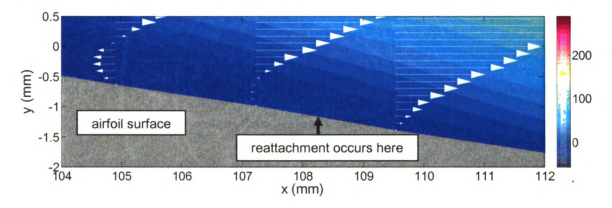


Figure 3.8: Mean velocity profiles near the reattachment point, overlaid on a velocity contour map. The units of the velocity contour "color scale" (displayed on the right) are mm/s. Every other vector is plotted in the cross-normal direction. Re = 40,000 and $\alpha = 5.49^{\circ}$ case.

Table 3.4: Separation and reattachment data for the cases investigated. A dash indicates that the flow did not reattach. Locations are normalized by the chord length. Uncertainty in separation and reattachment points is ± 0.0055 x/c.

| Re (× 10 ⁻³) | | | 20 | | |
|---------------------------|-------|-------|-------|-------|-------|
| alpha (°) | 3.75 | 5.65 | 7.30 | 8.80 | 10.55 |
| Separation (x/c) | 0.402 | 0.188 | 0.116 | 0.050 | 0.048 |
| Reattachment (x/c) | 0.994 | 0.901 | 0.888 | - | - |
| Bubble length (x/c) | 0.592 | 0.713 | 0.772 | - | - |

| Re (× 10 ⁻³) | | 30 | 40 | | | |
|---------------------------|-------|-------|-------|-------|-------|-------|
| alpha (°) | 3.49 | 7.39 | 3.59 | 5.49 | 7.29 | 10.44 |
| Separation (x/c) | 0.356 | 0.054 | 0.471 | 0.223 | 0.086 | 0.024 |
| Reattachment (x/c) | 0.936 | 0.438 | 0.807 | 0.526 | 0.311 | 0.144 |
| Bubble length (x/c) | 0.580 | 0.383 | 0.336 | 0.303 | 0.225 | 0.120 |

To analyze these results further, as well as to examine the trends exhibited, it is helpful to plot them in various ways. Figure 3.9 displays the separation and reattachment data as a function of angle of attack for the Reynolds numbers of 20,000 and 30,000 on the same axes. It is clear that as angle of attack is increased, the flow separates earlier, and asymptotically approaches a separation point close to the leading edge. As Reynolds number is increased, the separation point moves slightly upstream.

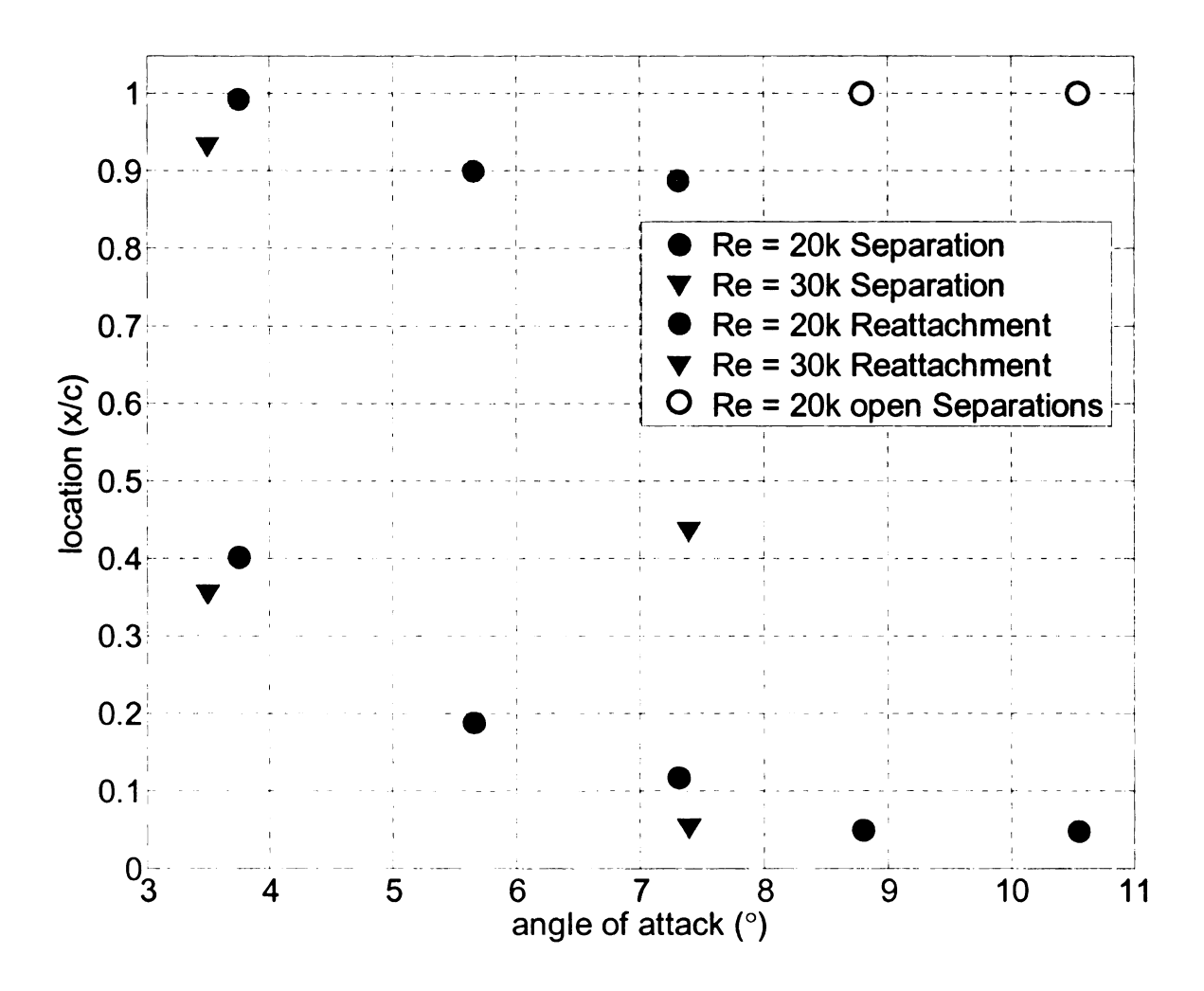


Figure 3.9: Separation and reattachment data plots for Re = 20,000 and Re = 30,000 for all measured angles.

When examining the reattachment of the Reynolds number of 20,000 cases, it is observed that for the three lowest angles of attack (3.75°, 5.65°, 7.30°) a closed LSB is formed. The reattachment point at an angle of attack of 3.75° is very near to the trailing edge of the airfoil, and moves slightly upstream as the angle is increased. At the highest angles (8.80°, 10.55) for this Reynolds number, the flow does not reattach over the airfoil surface. Although the separation and reattachment move upstream with increasing angle of attack, the bubble length increases with the angle.

This flow behavior can be compared with results from the literature. In general, results show that as the angle of attack is increased with constant Reynolds number, the LSB shortens and moves toward the leading edge [Galbraith et al., 2008]. Although the movement of the LSB upstream is observed in the TMUAL data, the bubble does not become shorter, and in fact grows. As angle of attack is further increased, it has been observed that the LSB can "burst" to form a longer bubble, and the stability of the smaller bubble is dependent on a wide range of external factors. Hysteresis is also observed, such that decreasing the angle of attack does not necessarily result in the smaller bubble reforming [Lissaman, 1983]. The open separations observed at Re =20,000 could be due to the LSB "bursting" and forming a bubble too large to reattach on the airfoil surface at these angles. Another possibility is that this behavior could be due to the effect of hysteresis. During the experiment, the mechanism by which the angle is varied on the airfoil rig (from low to high angle of attack) may overshoot the intended angle before being reduced to its final position. If a high enough angle of attack was reached that burst occurred before being reduced again to 8.80° or 10.55°, hysteresis effects may have prevented the smaller bubble from forming again at these angles. The reason for the bubble size increasing with angle of attack could be that the LSB is very near to the burst angle, and is already heading towards an open separation. These explanations are all in line with previous observations of low Reynolds number airfoil separation and reattachment.

In examining the data in which the freestream speed is increased for a Reynolds number of 30,000, the separation moves upstream and an attached LSB is formed in both angles tested. With the speed increased, the bubble length shortens, and the bubble length trend also changes. In contrast to the observed trend at Re = 20,000, at Re = 30,000 the LSB shortens with increasing angle of attack, which agrees with the trends found in the literature.

For further analysis, Figure 3.10 shows the separation and reattachment locations as a function of angle of attack for a Reynolds number of 40,000. This figure shows that every angle tested for this Reynolds number reattaches to form a closed LSB. In line with the previously shown results, the LSB shortens and shifts upstream towards the leading edge as the angle of attack is increased.

54

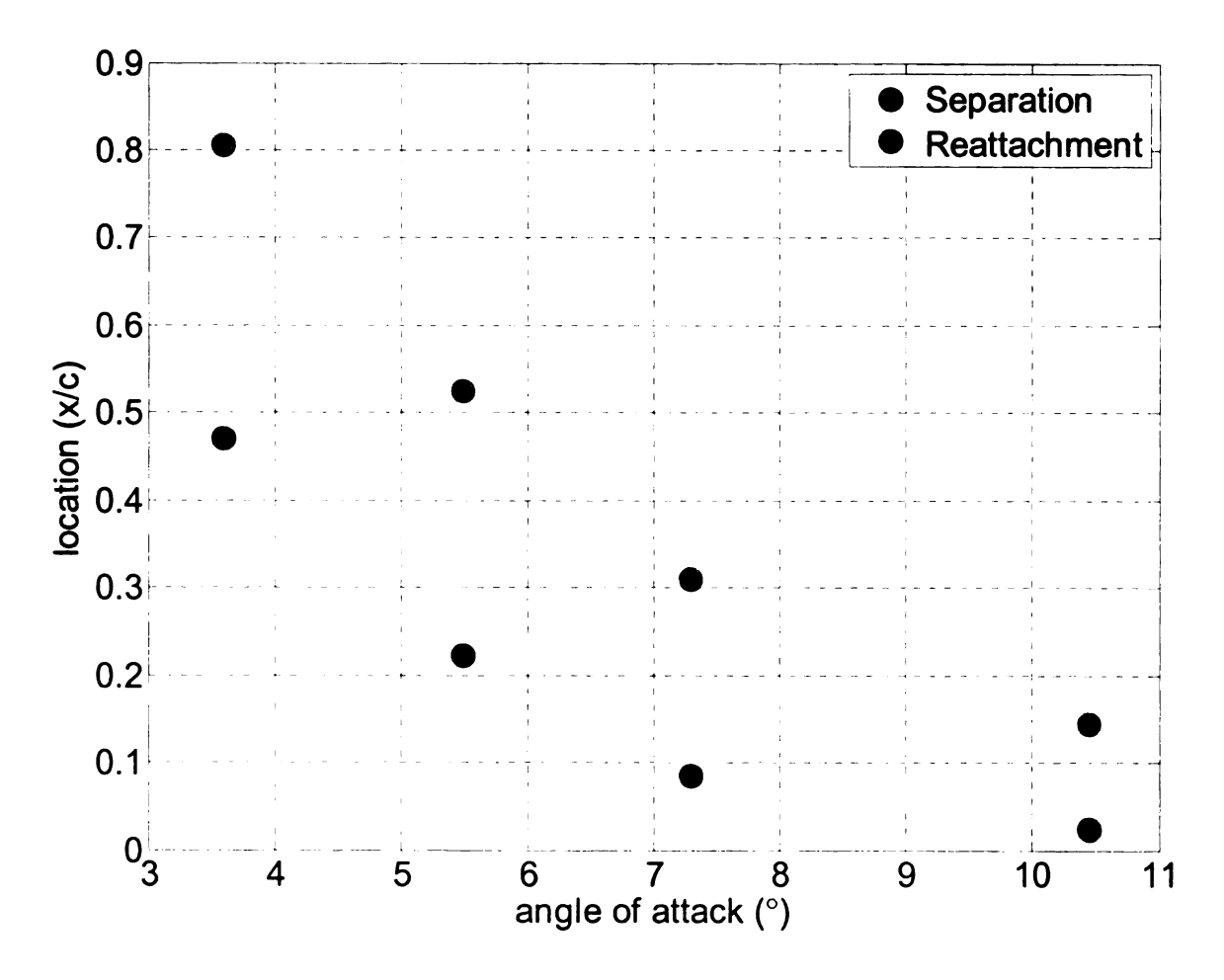


Figure 3.10: Separation and reattachment data for Re = 40,000.

Another useful way to examine the data is as a function of the Reynolds number, as there is clearly a strong dependence of the separation and reattachment on this parameter. Figure 3.11 shows the LSB results for $\alpha \approx 7.3^{\circ}$ for all three Reynolds numbers tested. This angle was chosen because the flow reattaches in all three cases, and the angles determined during post-processing were no more than 0.1° apart, so they can be compared easily. When examining the separation point, it seems to be roughly independent of the Reynolds number. However, there is a strong dependence of the reattachment point, and subsequently bubble length, on Reynolds number for a given

angle of attack. This figure clearly shows shortening of the LSB as Reynolds number is increased. This is likely due to more rapid transition of the shear layer to turbulence.

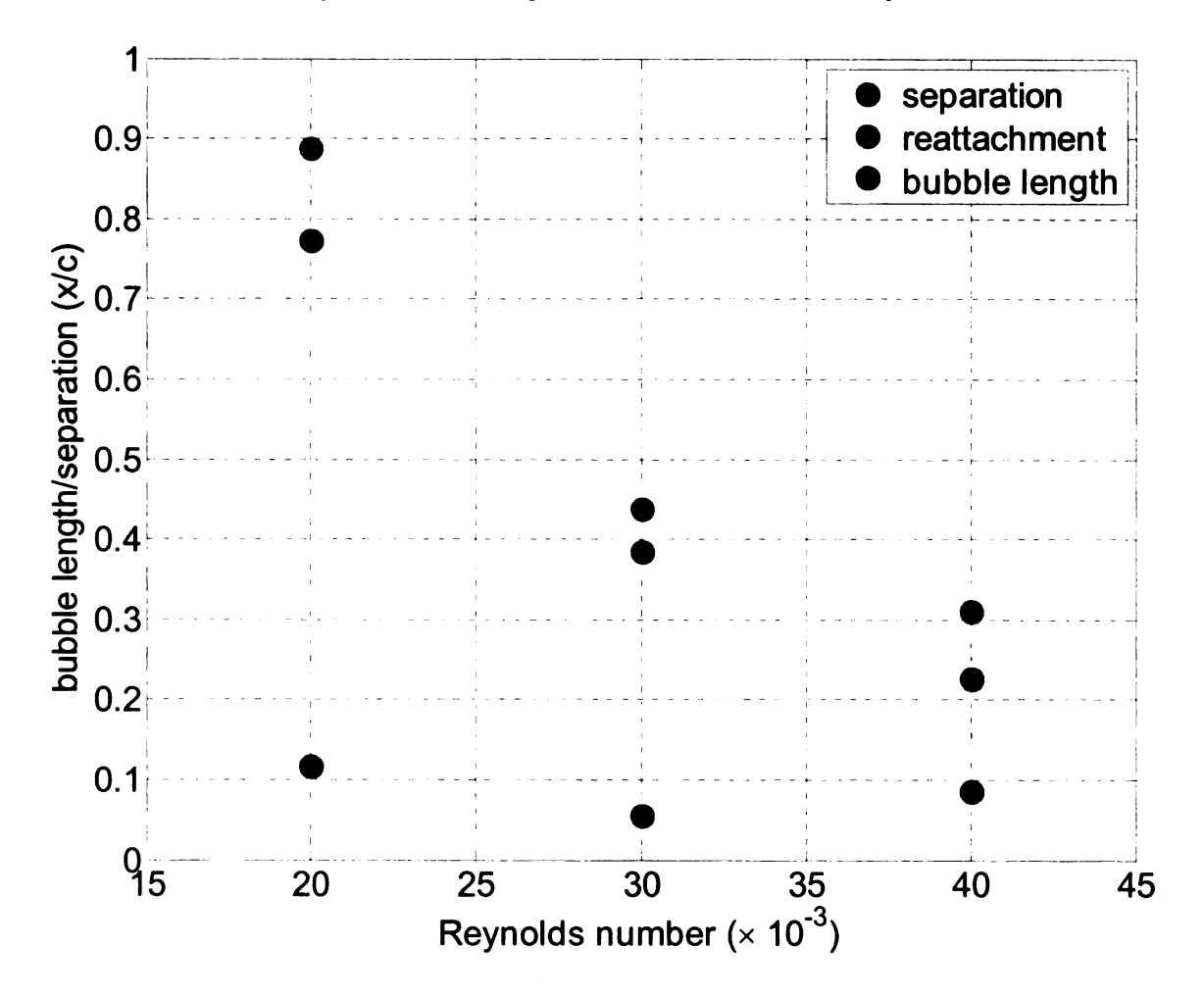


Figure 3.11: Separation, reattachment, and bubble length as a function of Reynolds number for $\alpha \approx 7.3^{\circ}$.

3.3. MEAN AND FLUCTUATION VELOCITY DATA

After investigating the separation and reattachment, the global behavior of the velocity and its fluctuations were then observed. In order to remain concise, and because results for different Reynolds numbers display similar trends, these results are only presented here in part. For all contour plots from these experiments, see Appendix A.

To see the evolution of the mean streamwise velocity (normalized by freestream) as a function of angle of attack, Figure 3.12 shows the mean velocity contours for all angles tested at Re = 40,000. Any contour levels below zero were manually set to bright yellow and the background has been set to gray so that the LSB is clearly identifiable. From this figure, upstream movement and shortening of the LSB with increasing angle of attack can be observed.

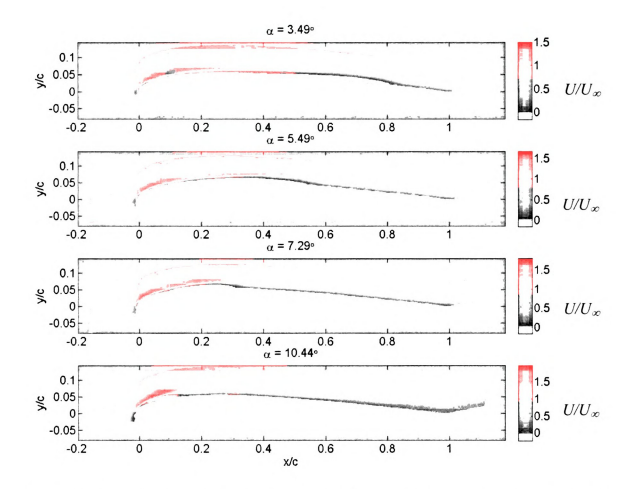


Figure 3.12: Evolution of normalized mean velocity $U\left(U/U_x\right)$ as a function of angle of attack for a Reynolds number of 40,000.

Similarly, the fluctuations (normalized) for these same cases are presented in Figure 3.13. When comparing these two figures, it is observed that the reattachment region of the separation bubble experiences the highest fluctuations, with a return to freestream level magnitude farther downstream. The return to freestream fluctuation levels occurs more rapidly with higher angle of attack. Also of note in these plots is the very small region of extremely high fluctuation near the leading edge of the airfoil. This is most visible for α = 10.44°. This is an artifact of the data processing, and there are two reasons this may show up in the data at that location.

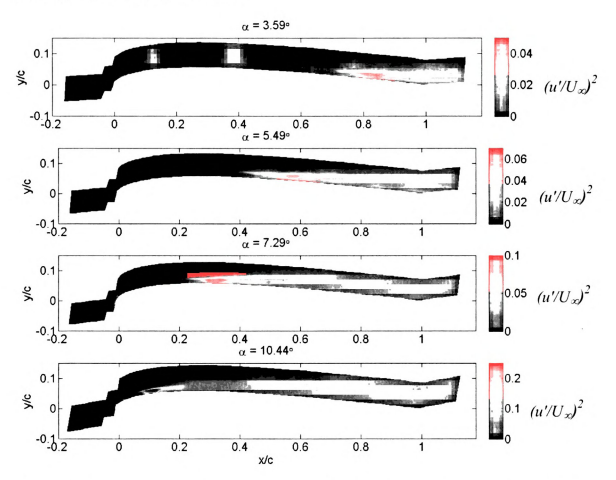


Figure 3.13: Evolution of fluctuations $((u'/U_x)^2)$ as a function of angle of attack for a Reynolds number of 40,000.

The combination of the flow acceleration and high spatial velocity gradient in this region causes the delayed image to have lines very close to each other. Thus, more than one peak may be inside the correlation window. A sample averaged image from near the leading edge is shown in Figure 3.14, and the intensities are extracted along the white line and plotted in Figure 3.15 to show the close proximity of the lines. When the lines are that close in proximity, the extracted intensity profile around the intended line may include peaks from neighboring lines, causing an erroneous correlation. Also observed is that the height of the peak is decreased in the regions of high gradient due to the "stretching" effect on the tagged line.



Figure 3.14: Average of 50 delayed images from the $\alpha = 10.44^{\circ}$ Re = 40,000 case. Intensities are extracted along the white line for display in Figure 3.15.

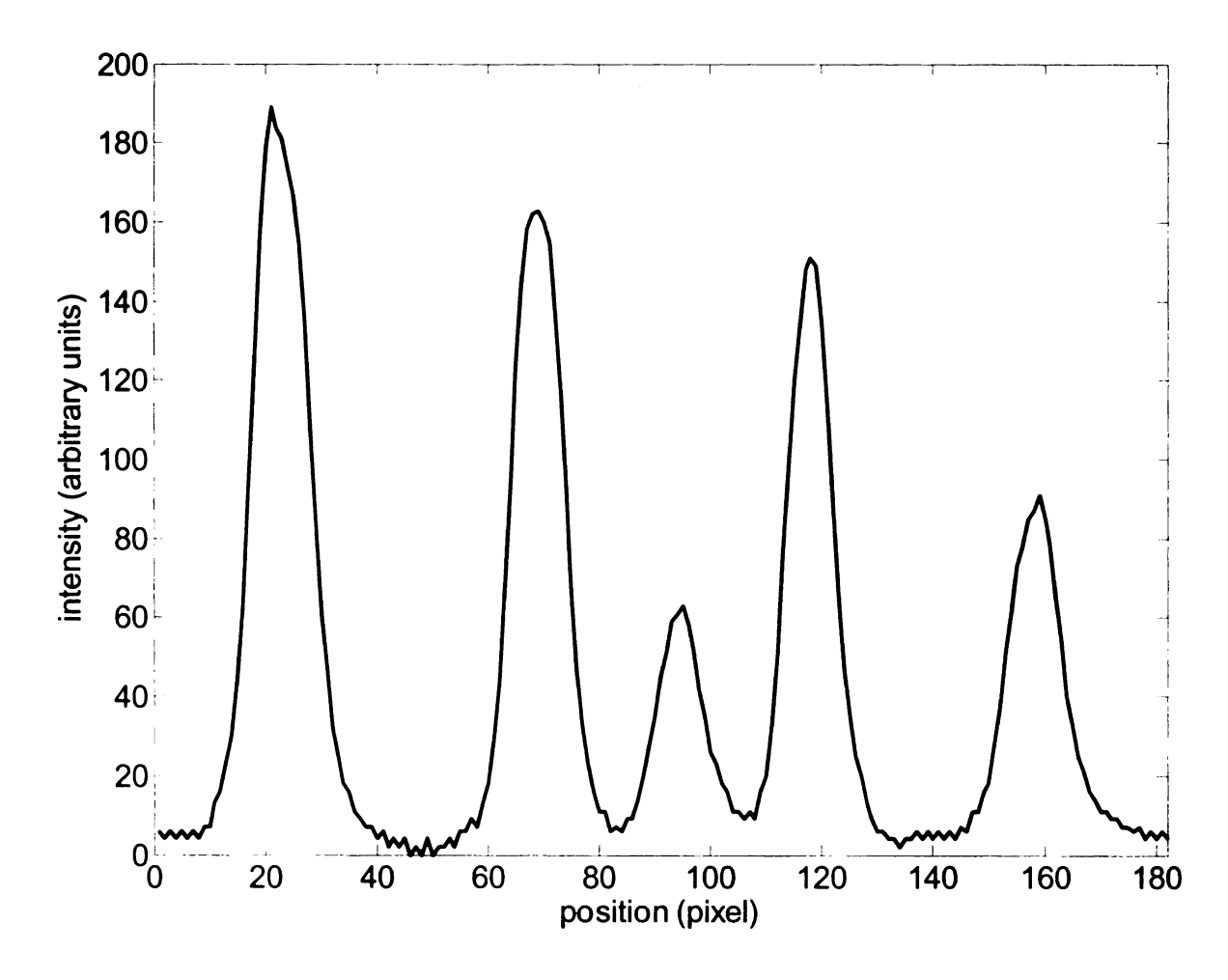


Figure 3.15: Intensity profile extracted along the white line from Figure 3.14 to highlight the close proximity of the peaks. Peaks as close as this can produce erroneous correlations in the processing technique.

Since it was also observed that the shape and location of the LSB is dependent on Reynolds number, the evolution of the LSB is investigated as a function of this parameter. Figure 3.16 shows the normalized (U/U_x) mean velocity for all three Reynolds numbers tested at a nominal angle of 3.5°. Again, the contour levels below zero were set to black for easy identification of the LSB. As Reynolds number is increased, the movement upstream and shortening of the LSB that was previously mentioned is observed. Though it is easy to observe the reattachment point as it moves upstream, the

LSB is so thin near the separation point that it is not easily observed in this figure due to the scale. In addition to this, the LSB height also decreases with increasing Reynolds number, a trend not seen before from the data presented thus far. This also agrees with the trends observed by Burgmann *et al.* [2007, 2008] (see section 3.4 for more details).

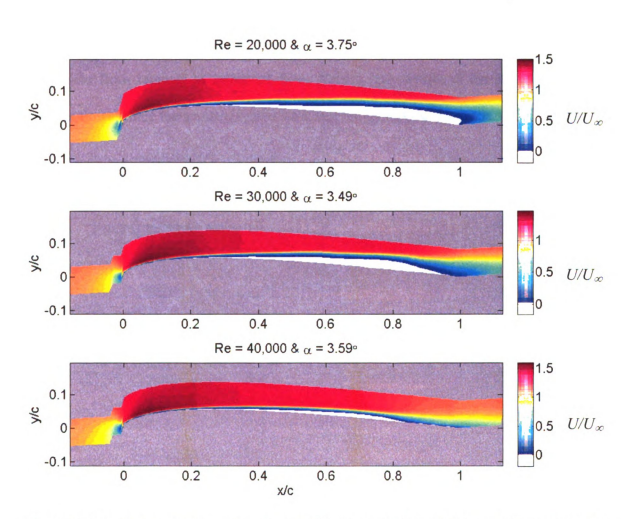


Figure 3.16: Mean *u*-component velocity (U/U_x) evolution with Reynolds number at a nominal angle of attack of 3.5°.

The evolution of the RMS as a function of Reynolds number also shows some interesting trends. Figure 3.17 shows that as the Reynolds number increases, the area of high fluctuation downstream of the LSB also becomes thinner and moves upstream. This region is observed over a larger portion of the airfoil at the lower Reynolds numbers, showing the longer bubble length. The lower Reynolds number cases also show a longer region of increasing fluctuations emerging from the separation point. This result is most likely caused by the instability of the separated shear layer as it moves downstream and transitions from laminar to turbulent flow. This is less visible in the higher Reynolds number flows, since the separation and transition occur farther upstream.

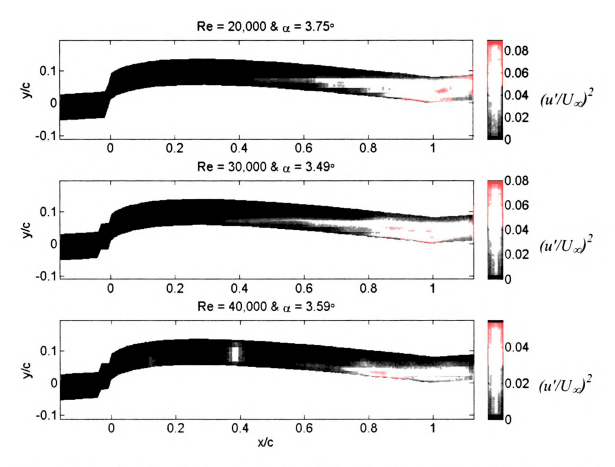


Figure 3.17: Evolution of normalized fluctuations of u $((u''U_x)^2)$ with Reynolds number at a nominal angle of attack of 3.5°.

3.4. LITERATURE COMPARISON

In order to evaluate and explain the results of the current experiments, other studies are considered for comparison. Previously, particle image velocimetry (PIV) measurements [Burgmann et al. 2007,2008] were made on an SD7003 model in a water tunnel at Reynolds numbers of 20,000 and 40,000, which makes them very good candidates for comparison. In addition to finding the separation and reattachment points of several cases, the height of the bubble was determined and time-resolved and three-dimensional data were acquired in these studies. The time resolved measurement shows that when a

closed LSB is observed, there exists high frequency ($O(10^0-10^1)$ Hz) vortex shedding at the downstream end of the bubble. After the flow has separated, the mechanism suggested in these studies to govern reattachment is the Kelvin-Helmholtz instability, which gives rise to the high frequency vortices. The three-dimensional (stereo-scanning) PIV measurements taken in the transition and reattachment regions also reveal the highly three-dimensional structure of the LSB and vortices.

For comparison, the separation and reattachment points for Reynolds number of 20,000 in the latest PIV measurements [Burgmann et al., 2008] are plotted in Figure 3.18 with the TMUAL results previously presented in this work. In examining this figure, it is observed that the TMUAL separation data agree very well with the PIV experiments, showing strong dependence on the angle of attack. The separation smoothly moves upstream with increasing angle of attack. On the other hand, the reattachment data for this Reynolds number differ greatly from those of the PIV measurements. There is a marked disagreement in the location of the reattachment, with the PIV measurements showing reattachment much further upstream than the TMUAL results. This indicates that there is likely a fundamental difference in the mechanism which is causing reattachment in the two experiments.

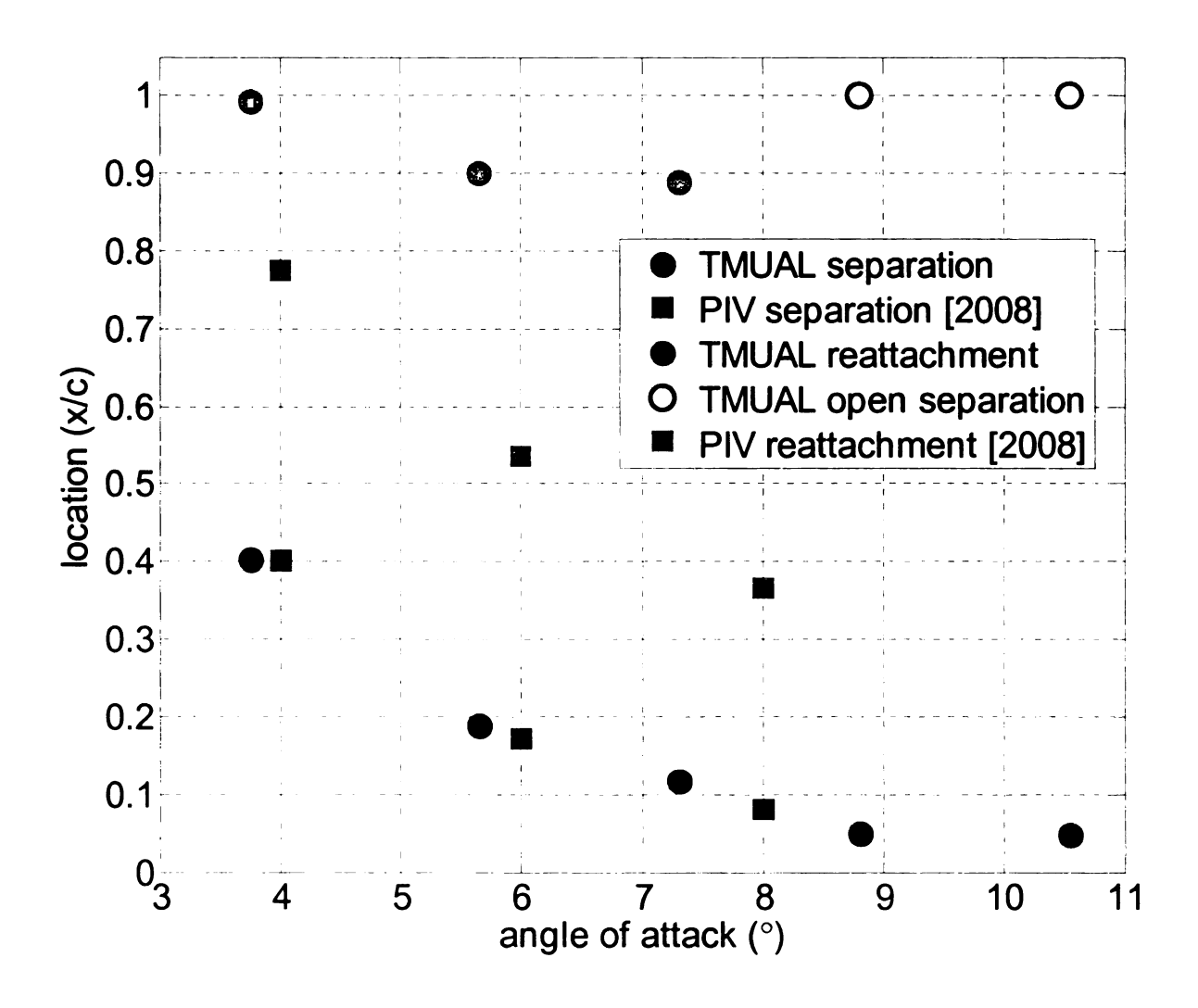


Figure 3.18: Separation and reattachment locations: Comparison between MTV (TMUAL) measurements and PIV [Burgmann *et al.*, 2008] measurements at a Reynolds number of 20,000.

One possible explanation of the reattachment point disagreement is the effect of freestream turbulence. Because disturbances present in the flow are amplified by the Kelvin-Helmholtz instability, higher freestream turbulence is posited to cause earlier transition to turbulence and subsequent reattachment. The effect of changing the turbulence level is observed by Burgmann *et al.* [2008], as their most recent experiments include additional flow conditioning devices that lowered the turbulence level to 1.0%

from 1.5% in the previous study [Burgmann et al. 2007]. The discussion of the effect of reducing the freestream turbulence level was limited to comments about the separation point and bubble thickness, offering little insight into the issue of reattachment. Looking at a comparison between the two Burgmann et al. studies in Figure 3.19, it is clear that the separation point has indeed shifted upstream in the experiments with decreased turbulence intensity, except in the case of an angle of attack of 8°. At high enough angle of attack this trend appears to be independent of freestream turbulence; i.e., the adverse pressure gradient is too severe for the flow to remain attached for both turbulence intensities.

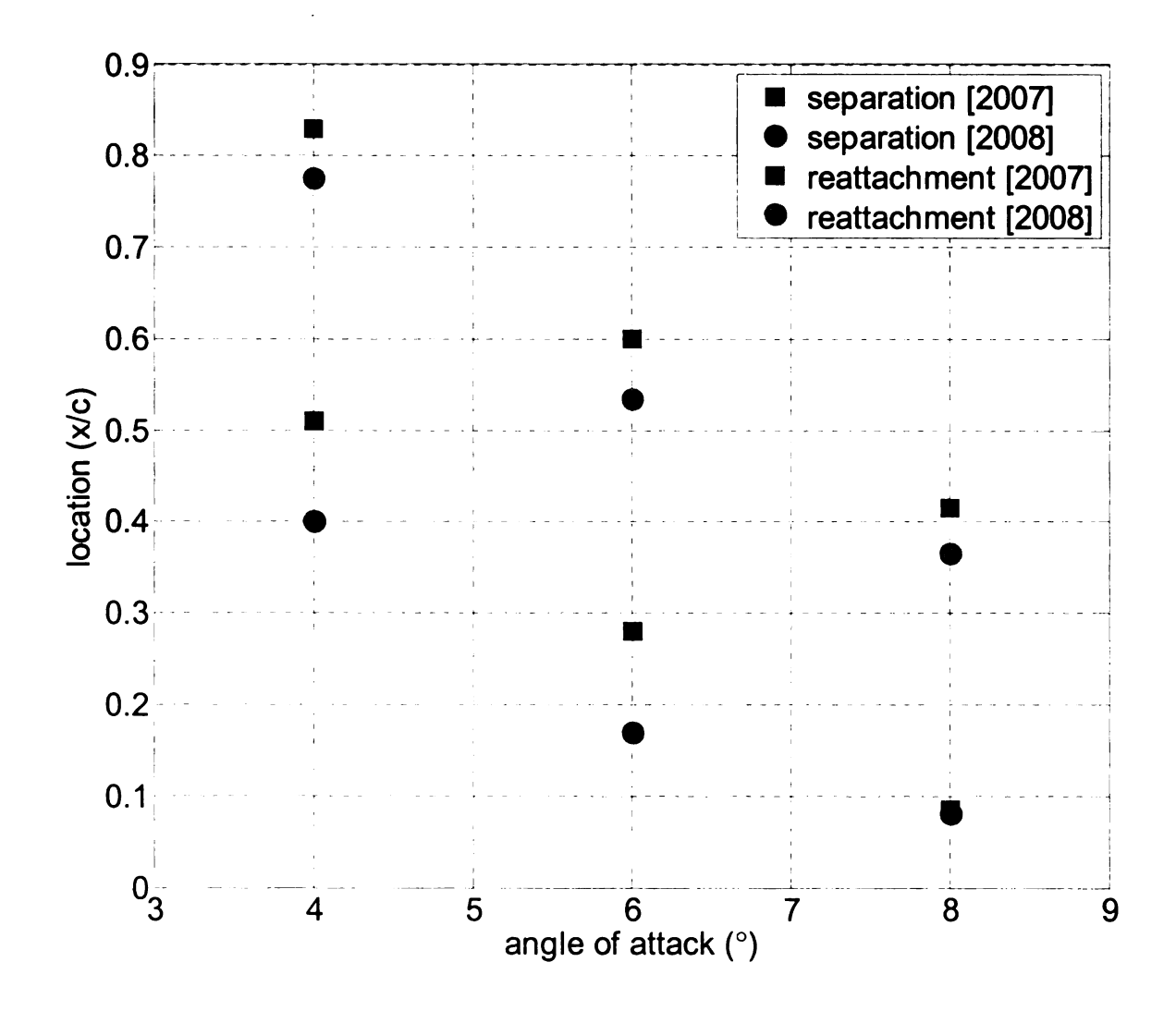


Figure 3.19: Effect of turbulence intensity on separation and reattachment points in PIV measurements. [Burgmann *et al.*, 2007, 2008]

From this figure, it also appears that the reattachment points have shifted upstream with the reduction in freestream turbulence in the same manner as the separation points. In the cases with α of 4° and 6°, although the reattachment point moves upstream, the LSB increases slightly in length (the reattachment moves downstream relative to the separation point). When the angle of attack is 8°, the recent measurements show the bubble has decreased in length. This does not clearly indicate the effect the freestream

[2008] PIV measurements used a method of determining the reattachment point that was fundamentally different from that in the previous publication. In the previous measurements, both the separation and reattachment points were determined using mean streamlines. In the recent measurements, the reattachment point was instead found instantaneously for every sample using the velocity v to differentiate between the LSB and the vortices at the downstream end of the LSB. This is noted by Burgmann *et al.* [2008] to result in a reattachment point further upstream than the method utilizing the mean streamlines. Thus, the observed reattachment points between the recent and previous PIV measurements can not be directly compared as a function of changing the turbulence level. It may still be possible, though not supported directly, that the freestream turbulence level has an effect on the reattachment.

Another possible explanation could be related to the spatial resolution of the measurements. The separation point is measured in the novel PIV experiments with an increased resolution, which may also account for some of the change from the previous PIV measurement. Although the spatial resolution of the TMUAL measurements was 5-8 times finer in the cross-stream direction than the resolutions of the quoted novel PIV separation measurements (0.0015c-0.0025c), agreement is still strong for the separation point. The resolution would likely not be a factor in the disagreement of the reattachment data, as the fundamental flow structure between the two sets of experiments seems to be different.

Therefore, the only supposition that can be made based on these results thus far is that both the TMUAL and PIV [Burgmann et al., 2008] measurements are spatially resolved "enough" to capture the separation points, as evidenced by comparing them as shown in Figure 3.18. The change in methodology in determining the reattachment points in the PIV experiments also does not allow direct comparison among these experiments. This means the freestream turbulence may still play a role in the reattachment process that is not fully understood. It is posited, but not directly supported, that decreasing the freestream turbulence of the PIV measurement facility even further may lead to open separations at higher angles such as those seen in the TMUAL experiments.

Yet another possible explanation for the striking disagreement in reattachment data is the spanwise features of the flow. Both SD7003 models are rectangular airfoils with a nominal chord length of 200 mm, although the airfoil used in the PIV experiments had a span of 300 mm, resulting in an aspect ratio of 1.5, as compared with the TMUAL model's aspect ratio of 2.25. Because the stereo-scanning PIV measurements indicate that the separated shear layer has a complex vortical structure that is highly three-dimensional, it is reasonable to expect that the reattachment process can be influenced by spanwise effects. Thus, the difference in aspect ratio could play a major part in comparing the data between the experiments in these facilities.

Figure 3.20 shows a comparison between the TMUAL and Burgmann *et al.* [2008] measurements of separation and reattachment points at Reynolds number of 40,000. The separation trend again agrees very well, while the reattachment data displays disagreement, though slight, similar to that observed in the Re = 20,000 cases. This

disagreement could also be due to spanwise effects of the highly three-dimensional flow, or differences in freestream turbulence between the flow facilities.

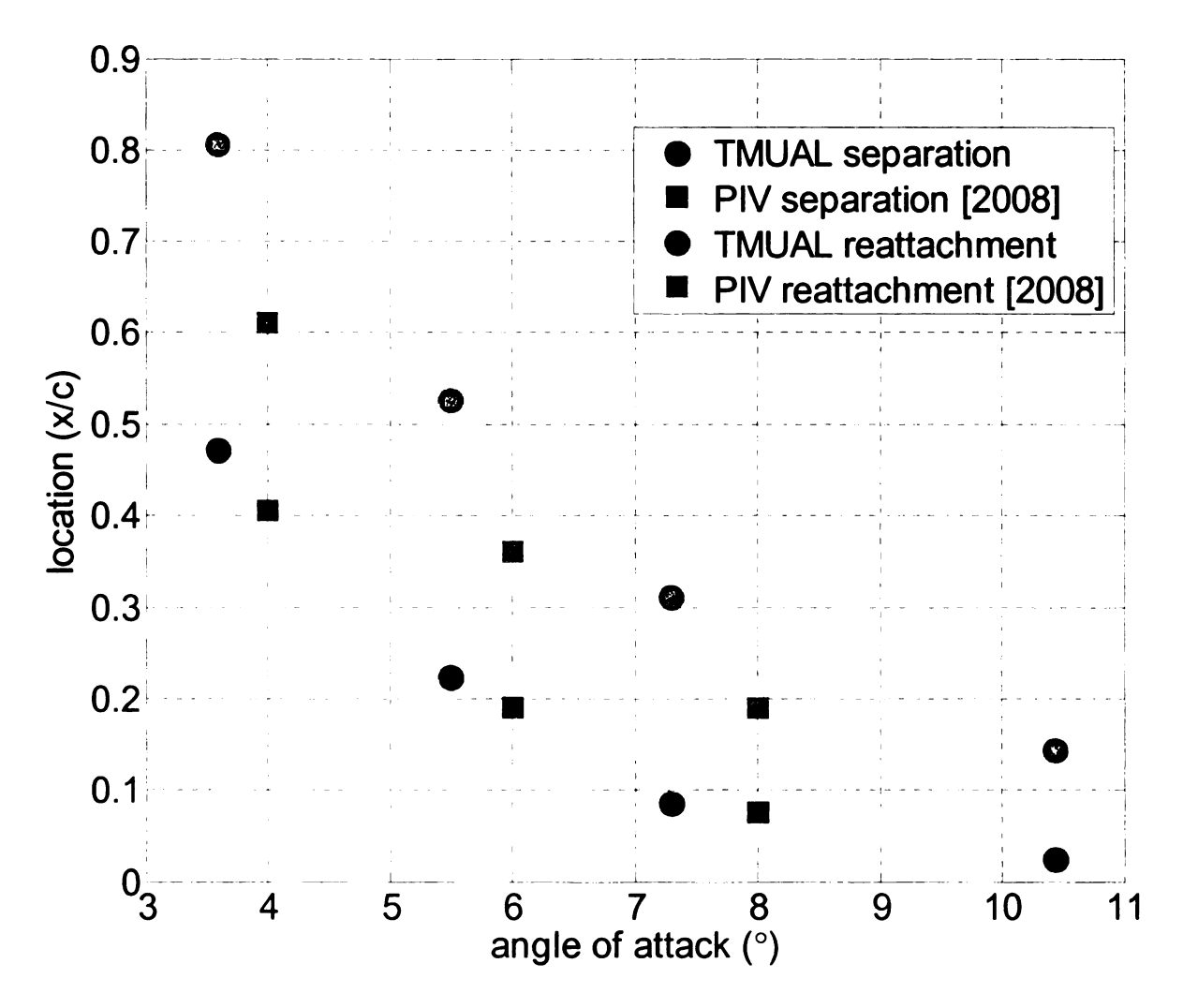


Figure 3.20: Separation and reattachment comparison between MTV (TMUAL) measurements and PIV [Burgmann *et al.*, 2008] measurements at a Reynolds number of 40,000.

Following the TMUAL data analysis in section 3.2, it is appropriate to also compare data as a function of Reynolds number to literature. For comparison, an implicit large eddy simulation (ILES) which investigates the SD7003 at various Reynolds numbers and

angles of attack [Galbraith et al. 2008] is chosen. Separation points for three Reynolds numbers are presented as a function of angle of attack in Figure 3.21 to observe any trends that are present. Two Reynolds numbers are represented by TMUAL data, while the third is represented by the data presented by Galbraith et al. [2008]. From this plot, it appears that the separation points fall into a wide band, with no clear dependence on Reynolds number.

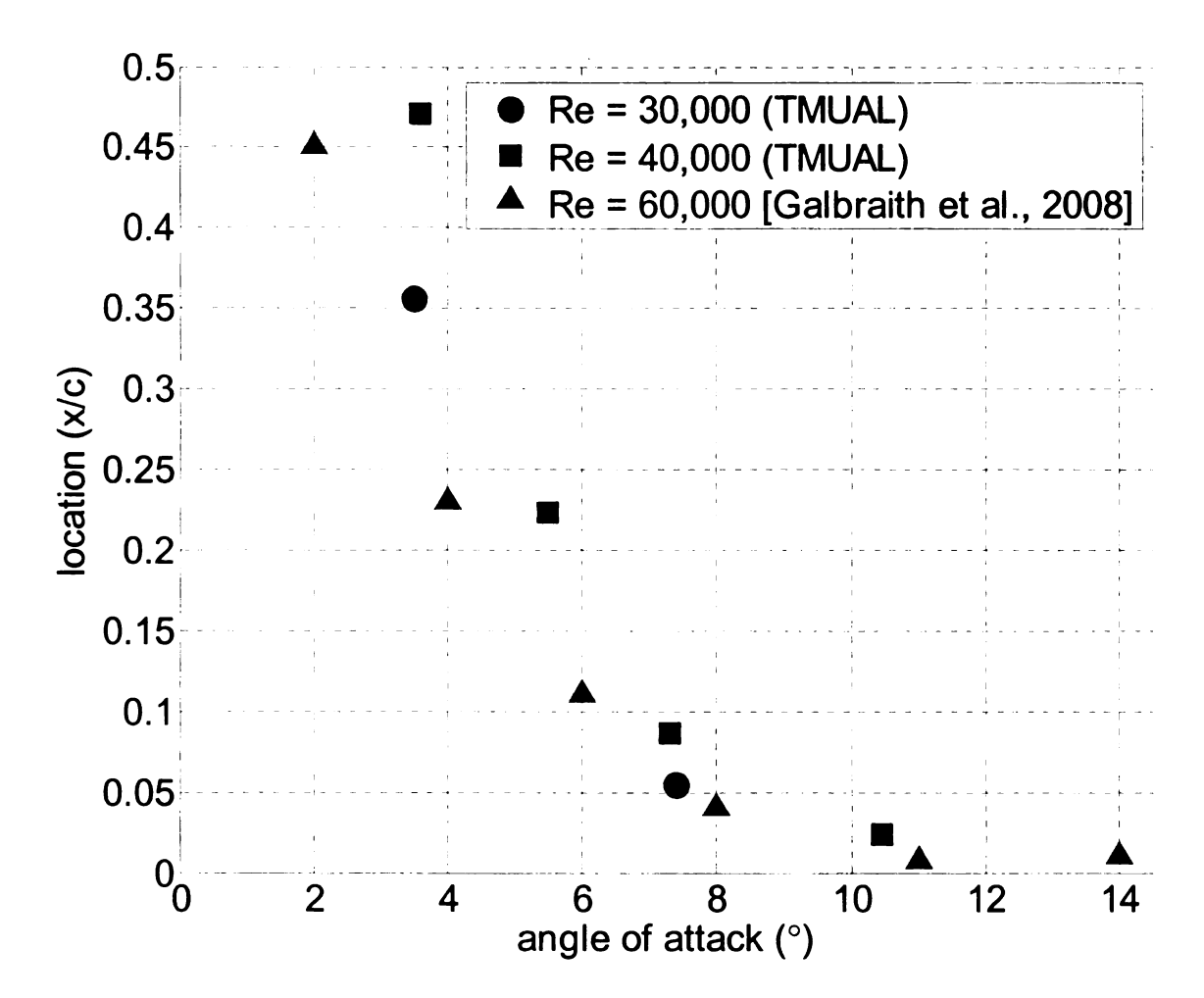


Figure 3.21: Separation point as a function of angle of attack for three Reynolds numbers.

The corresponding reattachment points for the above data sets are plotted in Figure 3.22. It is observed that the reattachment is independent of the Reynolds number above some threshold, with the reattachment shifting upstream as Reynolds number is increased.

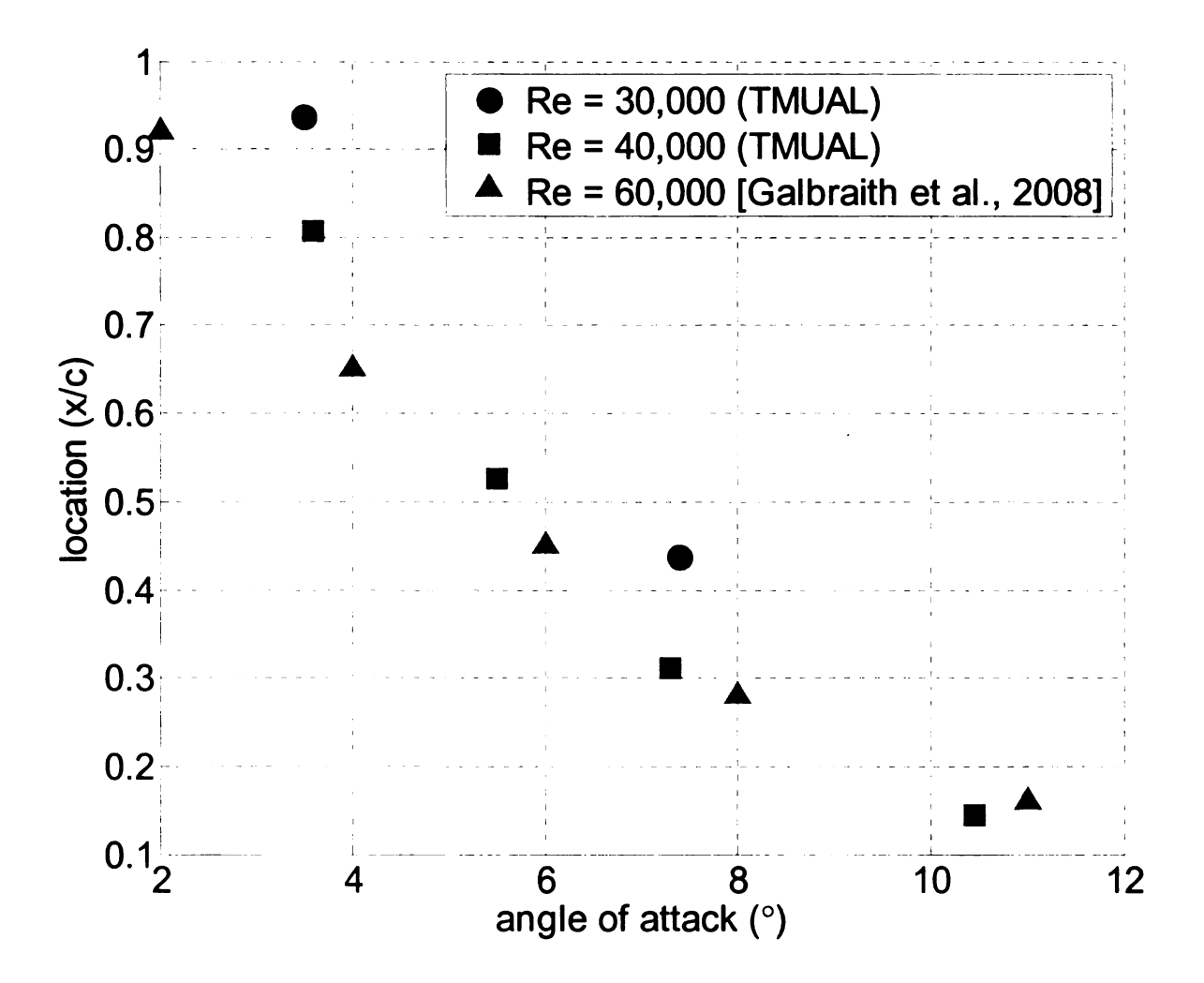


Figure 3.22: Reattachment point as a function of angle of attack for three Reynolds numbers

Though a wide range of parameters are investigated in the simulation by Galbraith *et al*. [2008], the particular angle of attack chosen for an investigation of the effect of Reynolds number was 8°. Because the TMUAL experiments do not include this exact angle, the

data must be interpolated. Because the form of the function that the data follows is unknown, two models were considered for use, a quadratic fit and a linear interpolation. These two models are compared in Figure 3.23, where they are applied to the separation and reattachment data for Re = 40,000.

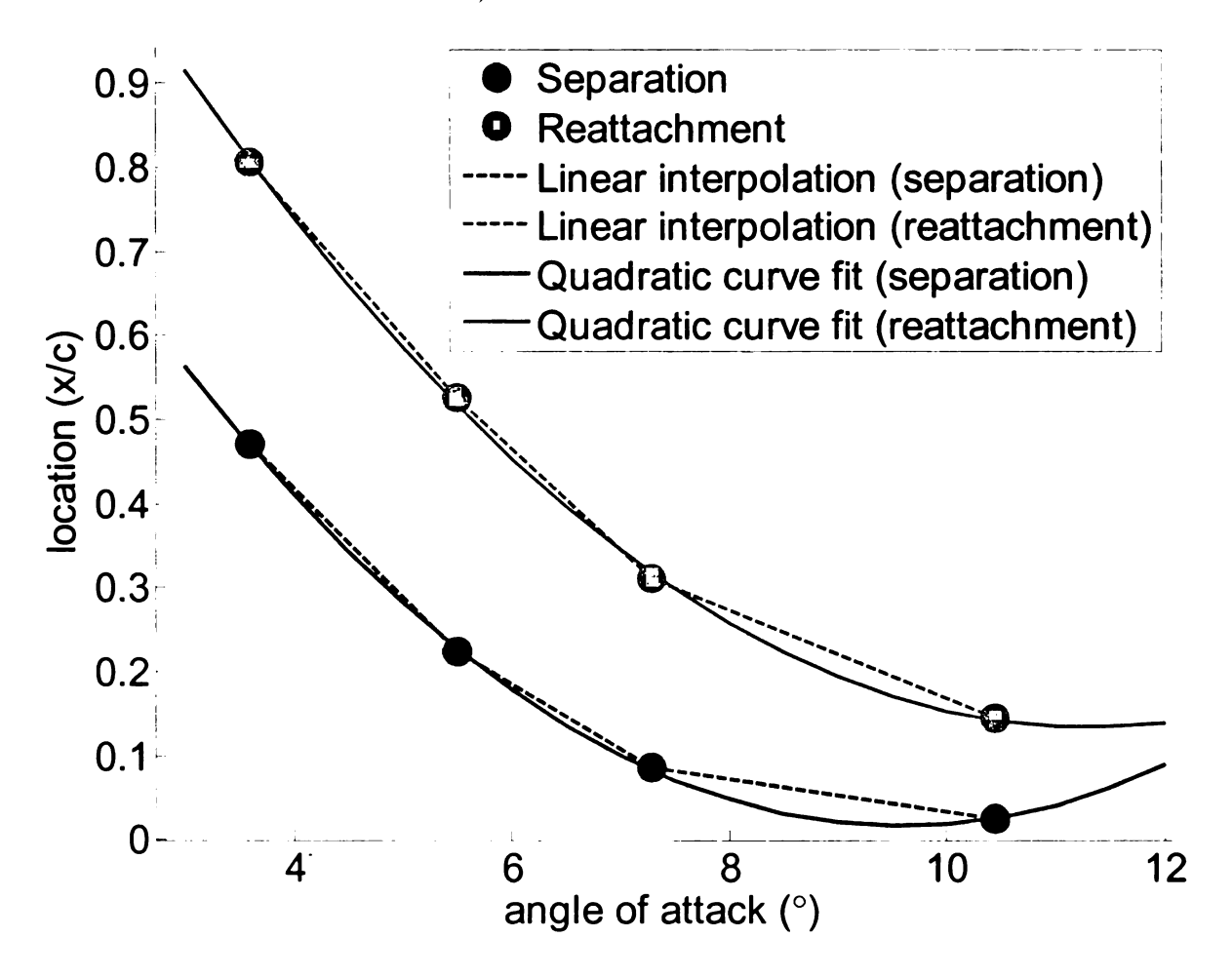


Figure 3.23: Comparison of quadratic and linear models for interpolating TMUAL data. Separation and reattachment are shown for a Reynolds number of 40,000.

Both models have their advantages and their drawbacks, and it is likely that neither is an exact fit for the data. The quadratic and linear models agree quite well at the lower angles, but when the curvature starts to change for the higher angles, the quadratic tends to underestimate the data, while the linear model tends to overestimate them. It is

speculated that this data will not have the change in slope that the quadratic fit, as observed in the separation data. For this reason and its simplicity, the linear model is chosen for interpolation. Thus, the TMUAL data presented in Figure 3.24 are linearly interpolated for a more direct comparison with the CFD data.

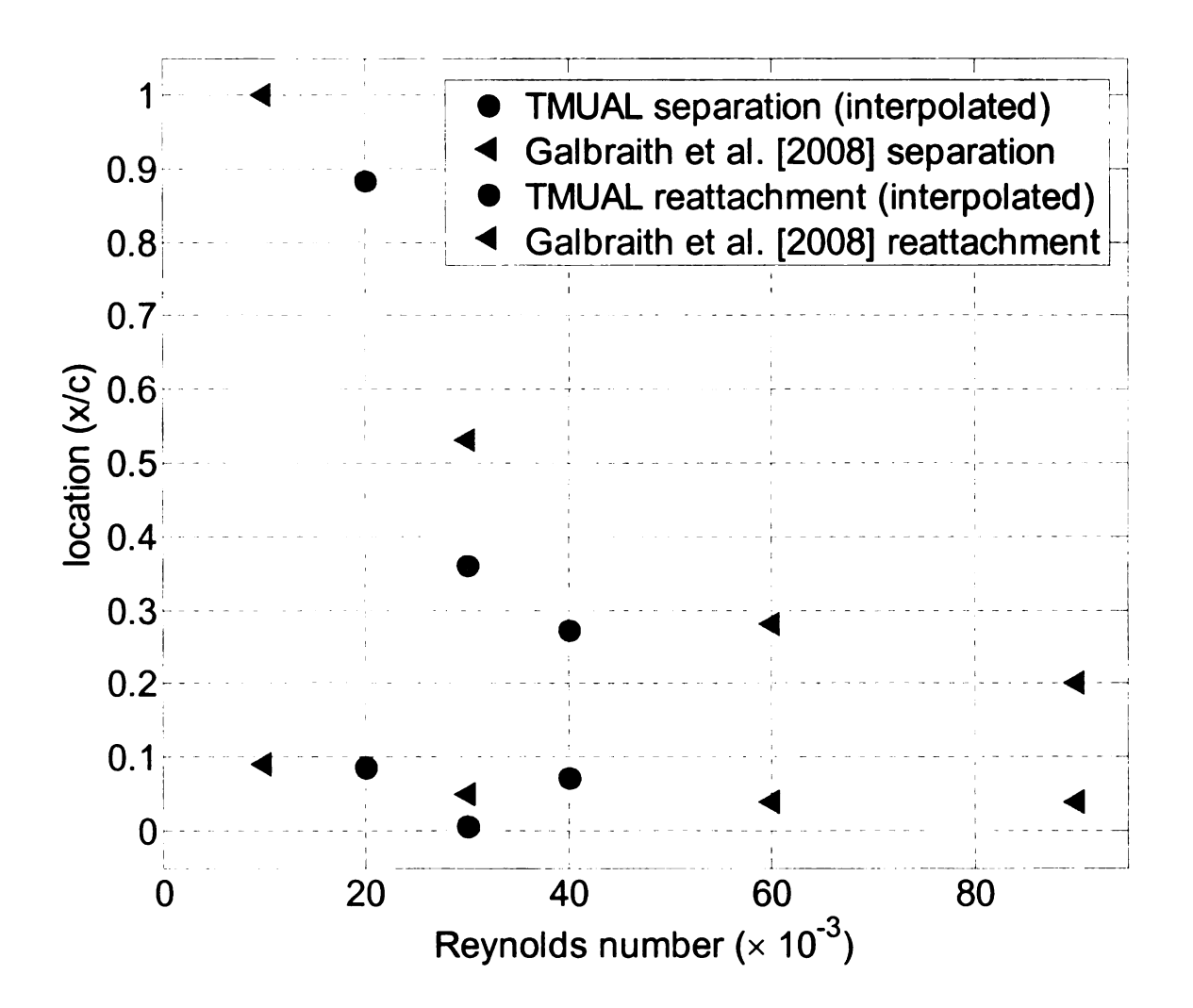


Figure 3.24: Comparison of TMUAL (interpolated) and ILES [Galbraith *et al.*, 2008] separation and reattachment data at an angle of attack of 8° as a function of Reynolds number.

The separation points show reasonably good agreement within the uncertainty of the measurements. The CFD results show that the separation moves upstream with increasing Reynolds number, although after the Reynolds number reaches 60,000, the separation appears to be independent of Reynolds number. With the earlier observations that separation becomes independent of angle of attack above a given angle, it is reasonable to assume that the separation point becomes independent of Reynolds number and angle of attack when the adverse pressure gradient is severe enough.

Although the reattachment points move upstream with increasing Reynolds number for both the TMUAL experiments and the simulations, there are some quantitative differences. The TMUAL results show a much steeper decreasing trend than that observed in the simulations. The same factors mentioned in the comparison to PIV measurements can be used for interpreting and comparing the data here as well. As previously mentioned, the span of the airfoil model being studied may play a major part in these results, due to the three-dimensional nature of the flow features being studied. Galbraith et al. [2008] investigated the effect of the spanwise extent in their simulations by running three simulations with angle of attack of 4° and Reynolds number of 60,000 while varying the spanwise extent. Three spans of 0.1c, 0.2c, and 0.3c were chosen for the investigation, and the three-dimensional structures, Reynolds stresses, and mean surface coefficient of pressure were compared between the three simulations. The three cases were observed to be very similar, such that the span of 0.1c was sufficient for the selected angle of attack and Reynolds number. However, due to the desire to study a wide range of (α, Re) combinations and the time of computation, a span of 0.2c was selected for robustness. This may seem to eliminate spanwise effects as a factor to consider when comparing different studies, but in fact it does not directly relate to either the TMUAL or PIV experiments. The goal of this investigation into the spanwise effects was to determine what span was needed in order to capture the turbulent motions in the flow. However, the boundary conditions of this flow are not comparable to those found in experiments. The span-wise boundary conditions are periodic, such that the simulation represents an infinite-span, two-dimensional geometry airfoil. In an experiment, there is either a wall or a wingtip at the boundary, since the airfoil model is actually a finite wing. Thus, this does not bring any new insight into the spanwise effects.

Another previously discussed factor is the freestream turbulence. In a simulation, unless turbulence is created artificially, the turbulence level is zero. In the case of these CFD simulations, no turbulence was added and the far-field boundary condition was prescribed to be freestream (except in the wake region). Since previous comparisons were inconclusive in determining the effect of turbulence intensity, it could still be playing a major role in the reattachment of the LSB.

To further compare with the CFD results, the mean velocity contours from the TMUAL data and the comparable CFD data are plotted in Figure 3.25. Once again, all negative contour levels are set to white to highlight the LSB. Note that the velocity u in the CFD results is in the airfoil coordinate system (not the same as defined in this work as the stream-wise velocity u), but the difference due to the rotation is less than 0.2%. In observing this figure, it is clear that the LSB in the CFD data is upstream compared with

that in the TMUAL. Part of this disagreement is likely caused by the slight angle of attack difference between the two data sets, since the LSB tends to shorten and move upstream with increasing angle of attack.

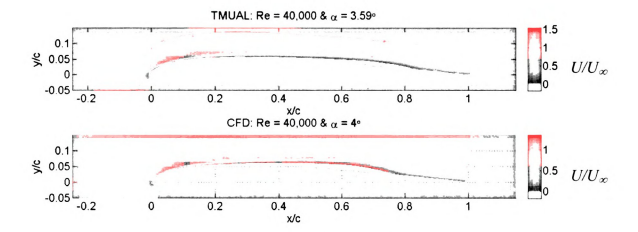


Figure 3.25: Normalized mean streamwise velocity (U/U_x) contour from TMUAL data, and normalized mean u contour (in airfoil coordinates) from CFD data.

The velocity fluctuation data corresponding to the same cases in Figure 3.25 are plotted in Figure 3.26. As has been previously observed, the regions of highest fluctuations occur just downstream of the LSB for both cases. However, the peak fluctuation value is lower for the TMUAL case than the CFD case, by about 0.02.

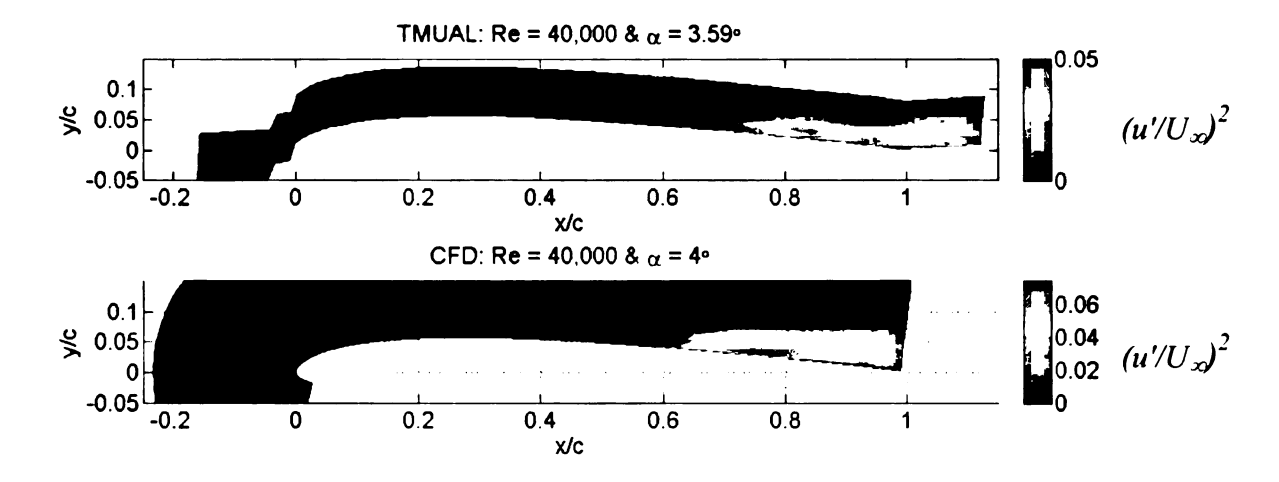


Figure 3.26: Fluctuation $((u'/U_x)^2)$ contours from TMUAL and CFD data.

This section outlined the comparison between TMUAL data and several literature sources. Separation point was found to be mostly independent of Reynolds number, but strongly dependent on angle of attack, and possibly strongly dependent on freestream turbulence. A wide variety of reattachment behavior was observed, and although a clear, strong, dependence on both Reynolds number and angle of attack was present, the full extent of the effects of span and freestream turbulence are not fully understood.

3.5. FUTURE WORK

The work described in this thesis provided a great deal of information about the low-Reynolds number flow around an SD7003 airfoil model using a molecular tagging velocimetry approach. Still left are questions regarding the cause of many large discrepancies between this and other works, as well as the effect of external variables on the flow. This section outlines future plans to address some of the unanswered issues that remain.

One important issue that still needs to be resolved is the bright spots that appear near the surface of the airfoil. Since the MTV technique relies on acquiring images after the laser pulse, the bright spots must be the result of some substance near or on the airfoil surface that is phosphorescing. In the early experiment mentioned briefly in this work, the bright spots were not present, so it is possible that the camera viewing angle of the airfoil surface or additional layers of marine epoxy caused an increase in the brightness on the surface. If the epoxy used is indeed phosphorescent, a different material that is inert, resistant to the tracer chemicals in the tunnel, and also does not emit light when excited by the laser will need to be found and used to coat the airfoil surface where measurements are to be made. This will help extract the near-wall velocity more accurately and may resolve some of the disagreements with the literature.

It is believed that many features of the LSB, especially the reattachment point (and subsequently the bubble length), are influenced by the freestream turbulence level. In future studies, grid-generated turbulence can be used to increase the turbulence level in the water tunnel. Different grids and different distances from a single grid could both be used to change the turbulence intensity and sweep through a range of turbulence levels. Once this range of intensities is calibrated and quantified, a set of velocimetry experiments would then be performed. LSB and other flow-field data could then be extracted.

Because it is also believed that spanwise effects of the airfoil model may play a role in the flow features, future studies should investigate the effect of changing the aspect ratio. This can be done by building a "false wall" that is able to slide in the span direction, varying the span and therefore the aspect ratio. Similar velocimetry experiments could then be performed for different aspect ratios.

APPENDIX

All contour plots of normalized mean velocity and normalized fluctuations, with curve fit applied, and contour levels below zero set to white.

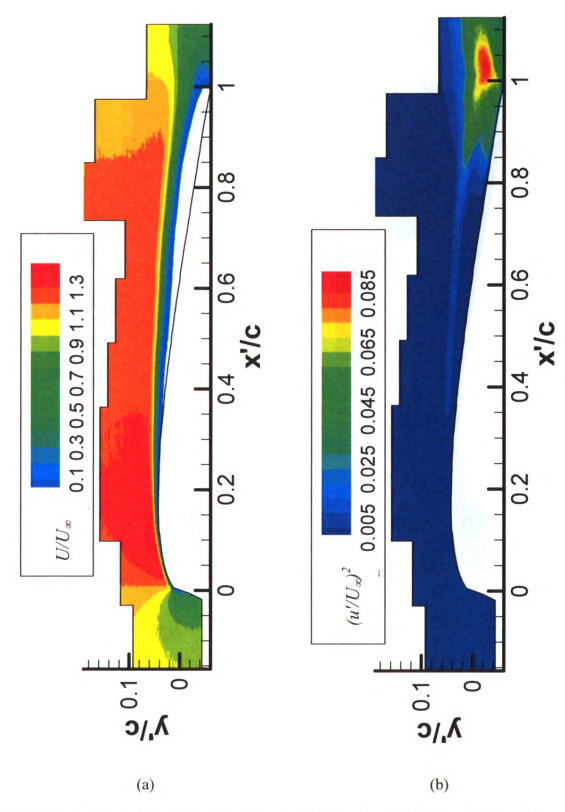


Figure A.1: (a) Normalized mean (U/U_x) and (b) fluctuation $((u/U_x)^2)$ of streamwise velocity component for $\alpha = 3.75^{\circ}$ and Re = 20,000.

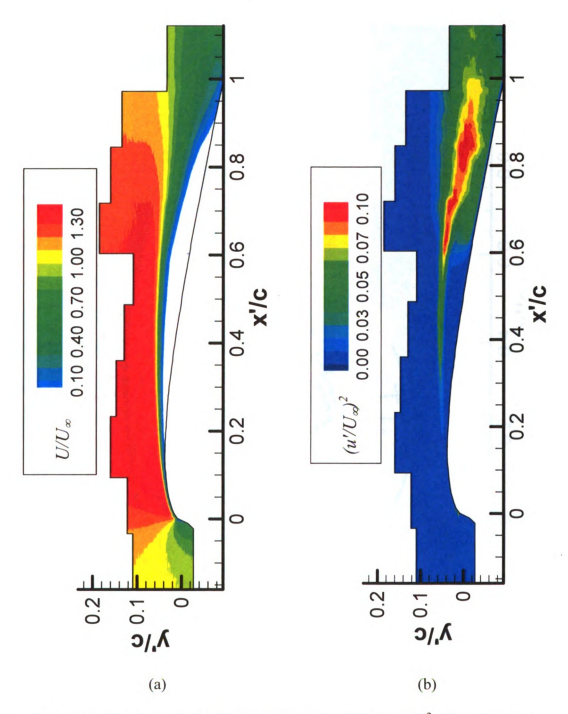


Figure A.2: (a) Normalized mean (U/U_x) and (b) fluctuation $((u/U_x)^2)$ of streamwise velocity component for $\alpha = 5.65^{\circ}$ and Re = 20,000.

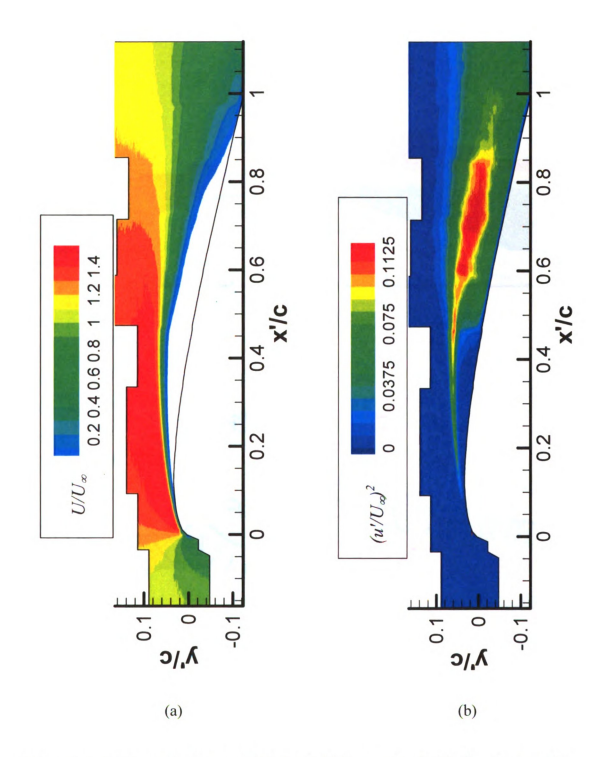


Figure A.3: (a) Normalized mean (U/U_x) and (b) fluctuation $((u/U_x)^2)$ of streamwise velocity component for $\alpha = 7.30^{\circ}$ and Re = 20,000.

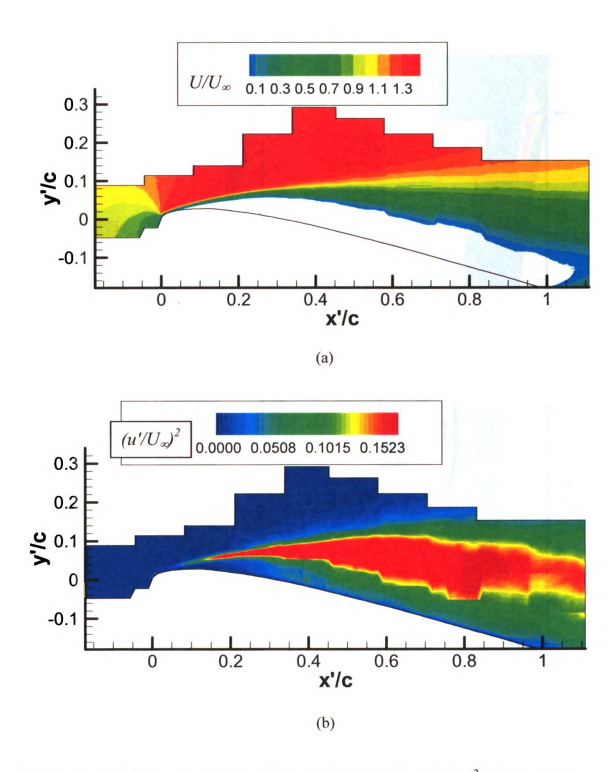


Figure A.4: (a) Normalized mean (U/U_x) and (b) fluctuation $((u/U_x)^2)$ of streamwise velocity component for $\alpha = 10.55^\circ$ and Re = 20,000.

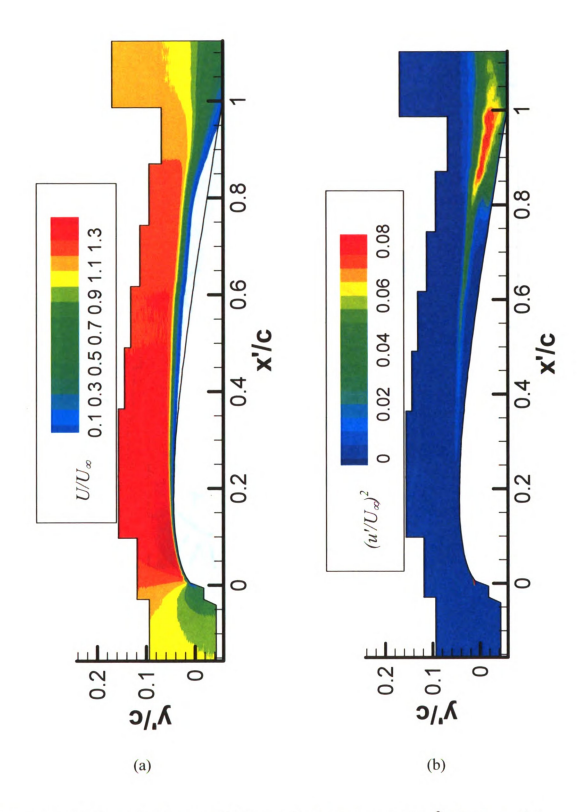


Figure A.5: (a) Normalized mean (U/U_x) and (b) fluctuation $((u/U_x)^2)$ of streamwise velocity component for $\alpha = 3.49^{\circ}$ and Re = 30.000.

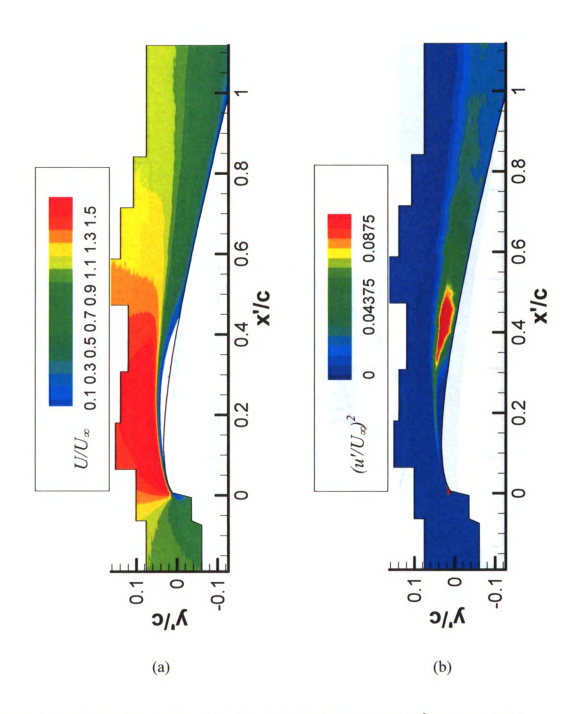


Figure A.6: (a) Normalized mean (U/U_x) and (b) fluctuation $((u'/U_x)^2)$ of streamwise velocity component for $\alpha=7.39^\circ$ and Re=30,000.

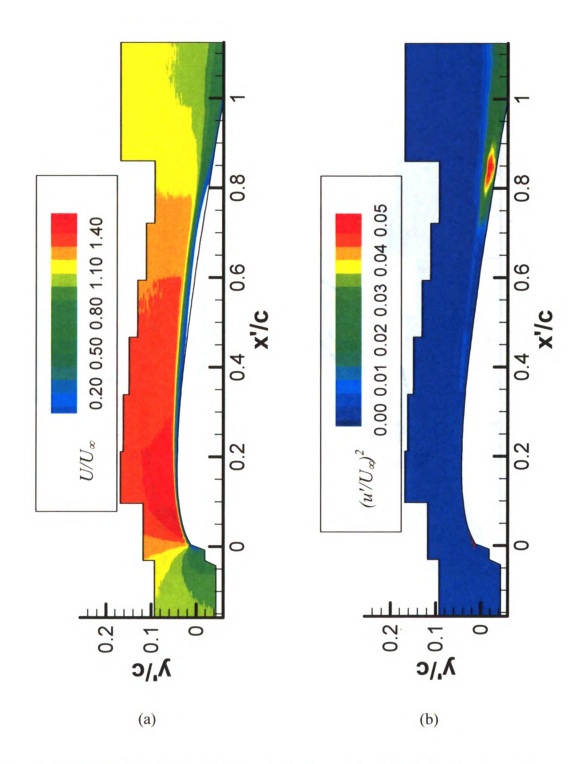


Figure A.7: (a) Normalized mean (U/U_x) and (b) fluctuation $((u'/U_x)^2)$ of streamwise velocity component for $\alpha = 3.59^{\circ}$ and Re = 40,000.

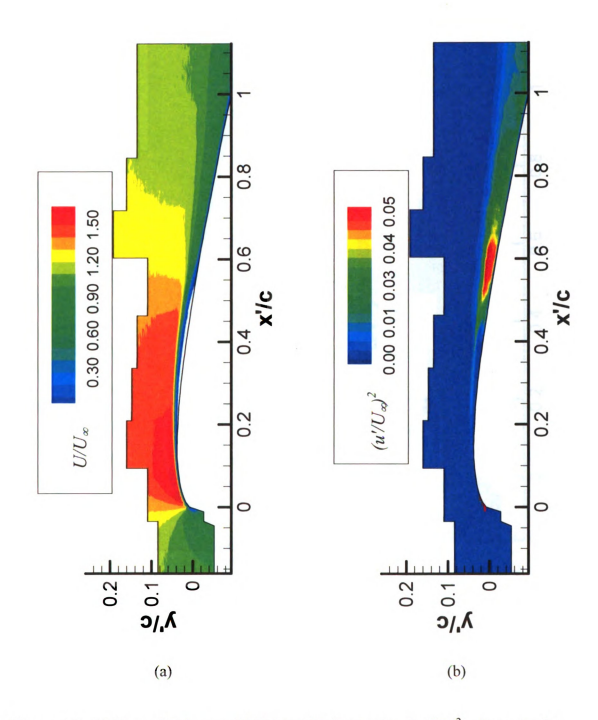


Figure A.8: (a) Normalized mean (U/U_x) and (b) fluctuation $((u'/U_x)^2)$ of streamwise velocity component for $\alpha = 5.49^\circ$ and Re = 40,000.

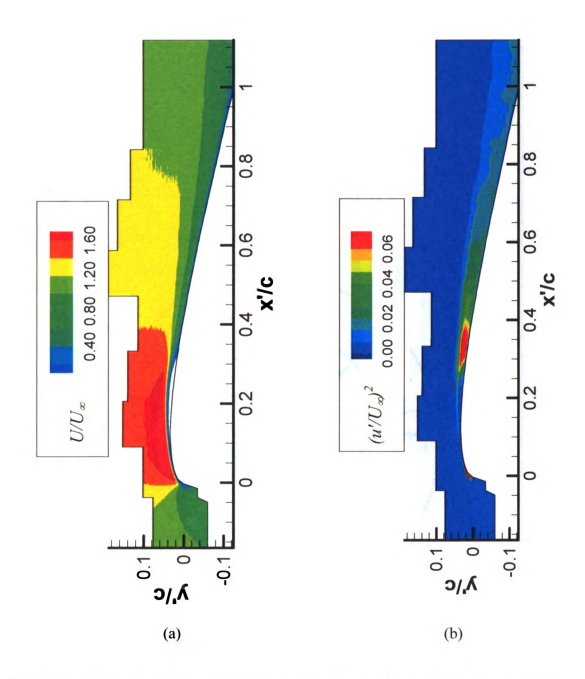


Figure A.9: (a) Normalized mean (U/U_x) and (b) fluctuation $((u/U_x)^2)$ of streamwise velocity component for $\alpha = 7.29^{\circ}$ and Re = 40,000.

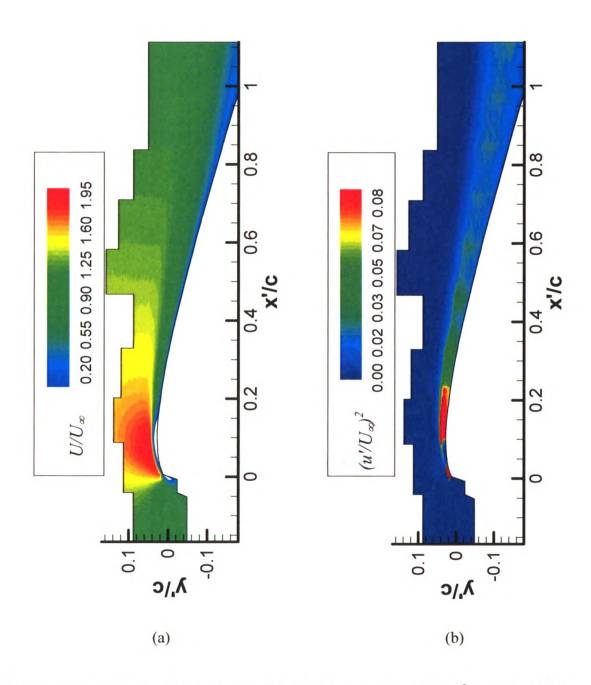


Figure A.10: (a) Normalized mean (U/U_x) and (b) fluctuation $((u/U_x)^2)$ of streamwise velocity component for $\alpha = 10.44^\circ$ and Re = 40,000.

REFERENCES

REFERENCES

- Bohl, D.G. [2002] "Experimental Study of the 2-D and 3-D Structure of a Concentrated Line Vortex Array". Ph.D. Dissertation; Michigan State University.
- Burgmann, S., Schröder, W. [2008] "Investigation of the vortex induced unsteadiness of a separation bubble via time-resolved and scanning PIV measurements". Experiments in Fluids 45, pp. 675-691.
- Burgmann, S., Dannemann, J., Schröder, W. [2007] "Time-resolved and volumetric PIV measurements of a transitional separation bubble on an SD7003 airfoil". Experiments in Fluids 44, pp. 609-622.
- Galbraith, M.C., Visbal, M.R. [2008] "Implicit Large Eddy Simulation of Low Reynolds Number Flow Past the SD7003 Airfoil". AIAA Aerospace Sciences Meeting an Exhibit. 7-10 January 2008, Reno, Nevada.
- Gendrich, C.P., Koochesfahani, M.M., Nocera, D.G. [1997] "Molecular tagging velocimetry and other novel applications of a new phosphorescent supramolecule". Experiments in Fluids 23, pp. 361-372.
- Hill, R.B., Klewicki, J.C. [1996] "Data reduction methods for flow tagging velocity measurements." Experiments in Fluids 20, pp 142-152.
- Koochesfahani, M. M. & Nocera, D. G. [2007] "Molecular Tagging Velocimetry". Handbook of Experimental Fluid Dynamics. Chapter 5.4.
- Lissaman, P.B.S. [1983] "Low-Reynolds-Number Airfoils". Annual Review of Fluid Mechanics 15, pp. 223-39.
- Ol, M. V., McAuliffe, B.R., Hanff, E. S., Scholz, U., Kähler, C. [2005] "Comparison of Laminar Separation Bubble Measurements on a Low Reynolds Number Airfoil in Three Facilities." 35th AIAA Fluid Dynamics Conference and Exhibit. 6 9 June 2005, Toronto, Ontario Canada.
- Selig, M.S. UIUC Airfoil Coordinates Database. University of Illinois at Urbana-Champaign. http://www.ae.illinois.edu/m-selig/ads/coord_database.html.

